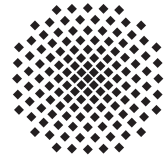




Universität Stuttgart
Geodätisches Institut



Marine Full Tensor Gravity Gradiometry Data Analysis and Euler Deconvolution

Studienarbeit im Studiengang
Geodäsie und Geoinformatik
an der Universität Stuttgart

Matthias Roth

Stuttgart, August 2009

Betreuer: Prof. Dr.-Ing. Nico Sneeuw
Universität Stuttgart

Erklärung der Urheberschaft

Ich erkläre hiermit an Eides statt, dass ich die vorliegende Arbeit ohne Hilfe Dritter und ohne Benutzung anderer als der angegebenen Hilfsmittel angefertigt habe; die aus fremden Quellen direkt oder indirekt übernommenen Gedanken sind als solche kenntlich gemacht. Die Arbeit wurde bisher in gleicher oder ähnlicher Form in keiner anderen Prüfungsbehörde vorgelegt und auch noch nicht veröffentlicht.

Ort, Datum

Unterschrift

The Euler Deconvolution is a standard tool of geophysical prospection. It is a semi automated process and supports the interpretation of magnet field data, gravimetry data or gravity gradiometry data. It is used to estimate the location of the source of a magnetic or a gravity field anomaly.

The obtained location may lead to a potential resource (e. g. petroleum, gas, ore, salt etc.)

Although gravimetry data or gravity gradiometry data are used in geodesy frequently this method did not attract much interest in this branch of science.

For this study thesis a real marine full tensor gravity gradiometry data set is given.

The data set was recorded by Bell Geospace. The gravity gradiometer was mounted on a ship. The measurement area lies between the Shetland Islands and the Faroe Islands. This area was chosen for the measurements because of the basalt formations there.

For geodesists the accuracy of data is of great interest. Therefore in a first step these data is run through an accuracy analysis.

After the introduction of the theory of the Euler Deconvolution and its testing on synthetic data the Euler Deconvolution is carried out on the data set.

The analysis of synthetic data shows that the Euler Deconvolution is suited to detect the location of a mass anomaly. If multiple mass anomalies are to be detected these mass anomalies must have a certain distance for this method to function reliably. If the distance between mass anomalies is too small the Euler Deconvolution tends to give false mass locations.

In spite of the big noise on the gravity gradient data the Euler Deconvolution still shows to be useful on the real data set.

Contents

1	Introduction	1
1.1	History	1
1.2	The gravity gradiometer of Bell Geospace	2
1.2.1	The Gravity Gradiometer Instrument (GGI)	2
1.3	Theory on gravity in short	3
2	Data analysis	6
2.1	Data record	6
2.1.1	Measurement area	6
2.1.2	Distances	7
2.2	Description of the data record	9
2.3	Testing of the Laplace equation	11
2.4	An example – <i>line 53</i>	14
2.5	Accuracy analysis of the measured data	16
2.5.1	Smoothed data	20
3	Euler deconvolution	24
3.1	Theory	24
3.2	Arranging Euler’s equation for gravity gradiometry data	25
3.3	Testing of the Euler Deconvolution	27
3.3.1	Determination of the centers of mass anomalies	27
3.3.2	Euler 2D	28
3.3.3	Euler 2D – added noise	29
3.4	Euler deconvolution with real data	30
3.4.1	Raw data	31
3.4.2	Smoothed data	31
3.5	Figures of the Euler deconvolution	32
4	Conclusions	49
A	Appendix	XII
A.1	Gradient tensor	XII
A.2	Data set	XII
A.2.1	Coarse analysis	XII
A.2.2	Crossover analysis	XIII
A.3	Euler Deconvolution	XIII
A.3.1	2D – synthetic data	XIII
A.3.2	Euler Deconvolution with real data	XIII

List of Figures

1.1	FTG system and GGI	3
1.2	Gravity gradient tensor of a point mass	5
2.1	Surveyed area	7
2.2	Bathymetry	8
2.3	Trajectories of the survey	9
2.4	Trajectories of the survey – detail	11
2.5	Estimated straight lines	12
2.6	Gravity gradiometry tensor components	13
2.7	Gravity components – T_{z1} and T_{ze}	13
2.8	Histogram of differences of Laplace’s equation	14
2.9	Line 53	15
2.10	Line 53 – T_{zz}	15
2.11	Crossing points	17
2.12	Histograms of the differences of the tensor components	19
2.13	Histograms of the differences of the combined tensor components	20
2.14	Line 53 smoothed	21
2.15	Histograms of the differences of the smoothed tensor components	22
2.16	Histograms of the differences of the combined smoothed tensor components	23
3.1	Chosen trajectories for Euler deconvolution.	31
3.2	Single point mass anomaly, positive $\Delta\rho$	33
3.3	Single point mass anomaly, negative $\Delta\rho$	33
3.4	Two point masses.	34
3.5	Three point masses.	34
3.6	Four point masses.	35
3.7	Four point masses, second to the right with negative $\Delta\rho$	35
3.8	Five strongly lumped point masses.	36
3.9	Five masses with the same size and at the same depth.	36
3.10	One point mass, 10% noise, window size of 641 samples.	37
3.11	One point mass, 10% noise, window size of 1281 samples.	37
3.12	One point mass, 10% noise, window size of 2561 samples.	38
3.13	Five point masses with same size, different depth, noiseless, window size of 641 samples.	39
3.14	Five point masses with same size, different depth, 10% noise, window size of 641 samples.	39
3.15	Five point masses, size bigger with depth, 10% noise, window size of 641 samples.	40
3.16	Two point masses, 10% noise.	41
3.17	Two point masses, different noise at 10%.	41
3.18	Two point masses, 20% noise.	42

3.19	Two point masses, 30% noise.	42
3.20	Two point masses, $n = 0.5$	43
3.21	Two point masses, $n = 1$	43
3.22	Two point masses, $n = 2$	44
3.23	Two point masses, $n = 3$	44
3.24	Raw data, <i>line 53</i> , window size of 1001 samples.	45
3.25	Raw data, <i>line 54</i> , window size of 1001 samples.	45
3.26	Raw data, <i>line 65</i> , window size of 1001 samples.	46
3.27	Raw data, <i>tie 40</i> , window size of 1001 samples.	46
3.28	Smoothed data, <i>line 53</i> , window size of 1001 samples.	47
3.29	Smoothed data, <i>line 54</i> , window size of 1001 samples.	47
3.30	Smoothed data, <i>line 65</i> , window size of 1001 samples.	48
3.31	Smoothed data, <i>tie 40</i> , window size of 1001 samples.	48

List of Tables

2.1	Small sample of the data set.	10
2.2	Cross-over analysis of measured data	18
2.3	Analysis of measured data	18
2.4	Cross-over analysis of smoothed data	21
3.1	Structural indices for usage with gravity gradiometry data (Blakely, 1995).	25

Chapter 1

Introduction

It is nowadays somewhat unlikely that new mineral resources near to the surface of the earth will be found very often. Such mineral resources then are often found in quantities which are not minable.

Therefore nowadays the search broadens for resources which are located deeper in the earth (e. g. the search for petroleum and gas in the deep sea). But the costs to find such resources are very high. Especially resources at the ground of the ocean are hard to find and even more costly to mine.

With the Euler Deconvolution a suitable method exists to extract the locations of such resources out of magnetic, gravity or gravity gradiometry data. To measure the data and perform an Euler Deconvolution is more economic than to drill boreholes and getting material samples while covering an entire area (in the deep sea especially).

With Euler Deconvolution it is possible to detect promising locations and then to place boreholes only there.

1.1 History

The gravity gradient tensor gives valuable information about the local gravity field. This information plays an important role for several topics in geodesy and geophysics.

The principle of gravity gradiometry has been known for more than 100 years. First accurate measurements were made in the 1920th with a torsion balance improved by Loránd Eötvös. Measurements done with a torsion balance are very time consuming, because of the slow swinging probes and the complexity of the measurement procedures. Because of the small measurement quantities the accuracy requirements are high. A lot of supplementary measurements like levelling of the directly surrounding terrain or temperature measurements must be taken into account to correct the measured gravity gradient values (Torge, 1989).

In the 1970s Bell Aerospace (now Lockheed Martin) developed a gradiometer instrument which was first used by the US Navy to determine differences in density within the watercolumn caused by nearby submerged objects or for bathymetry (Murphy, 2004).

Shortly afterwards the potential of the gradiometer instrument for tasks in exploration was recognized and Full Tensor Gravity Gradiometers (FTG) were built. The biggest advancement of these FTGs is the possibility to do measurements of gravity gradients in a much quicker way. Also the devices need not to be stationary during a measurement. So it became possible to

mount a gravity gradiometer on a moving platform and therefore to get continuous measurements.

1.2 The gravity gradiometer of Bell Geospace

This section is mostly based on the description given by Bell Geospace (2009) and Murphy (2004).

Bell Geospace owns three full tensor gravity gradiometry systems. These systems are applicable for airborne FTG (Bell Geospace calls it *Air-FTGTM*) where a FTG system is mounted on an aircraft or for ship mounted FTG (called *Marine-FTGTM* by Bell Geospace).

A FTG system (see figure 1.1 bottom left) consists of three gravity gradiometer instruments, which are mounted at an angle of 120° towards each other and at the same time are inclined at an angle of 35.26° from the horizontal. (See figure 1.1 bottom right).

1.2.1 The Gravity Gradiometer Instrument (GGI)

The main component of a gravity gradiometer instrument is an disk rotating at a specific rate on which four accelerometers are mounted. The accelerometers are arranged in two pairs. The accelerometers of one pair are positioned diametrically 15 cm apart on the disk. The other pair is mounted in a similar manner at a right angle to the first (see figure 1.1 top). The scale factor of the opposite accelerometers must be matched precisely.

This assembly is beneficial. Acceleration effects are caused by current or the vehicle (e. g. vibrations of the motor). These effects can be reduced because of the fast rotating disc and the continuous data gathering. Also it is possible to minimize long-term effects e. g. caused by a temperature drift in the electronic components.

Problematic is the so called red noise (noise at low frequencies). It is not easy to distinguish red noise from the actual signal. This problem could be solved by the assembly of the accelerometers on the fast rotating disk as the measured gradient signal will be shifted to a higher frequency. Therefore the signal can be separated from red noise easily.

The GGIs are mounted on a gimbal stabilized platform. In inertial navigation, as applied to ships and submarines a minimum of three gimbals is needed to allow the platform to remain fixed in inertial space, compensating for the ship's *yaw* (direction, azimuth) as well as its *pitch* and *roll*.

For measurements with marine FTG the azimuth gimbal rotates with a specific rate to reduce noise. (For measurements with airborne FTG the gimbal does not rotate but is turned by an angle of 120° on consecutive survey days for improved noise reduction).

The measured gradients are computed of the differences of the readings between the two accelerometers of a pair.

The output of all four accelerometers is added to get the acceleration of gradients without linear accelerations. The data sample rate is 128 Hz.

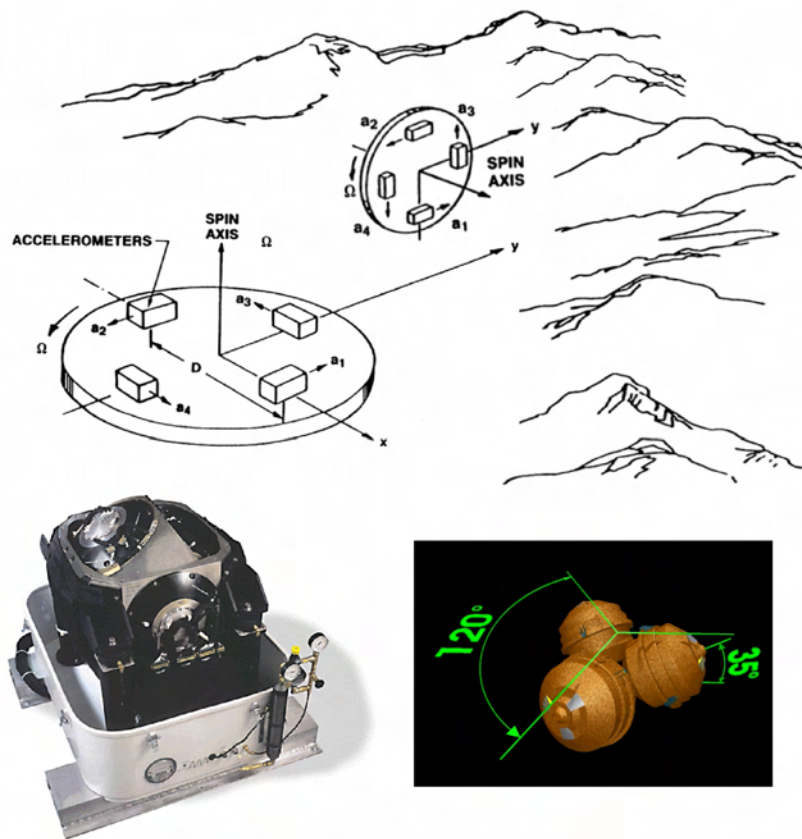


Figure 1.1: Top: A rotating disk with four accelerometers is the main component of a Gravity Gradiometer Instrument. Bottom left: FTG system. Bottom right: Principle of arrangement of the three GGLs (Murphy, 2004).

This data is processed further to obtain the actual gravity gradient tensor data at the measurement points as given in the data set.

1.3 Theory on gravity in short

We will use gravity gradient tensors in this study thesis frequently, so a short overview on the formulas should be presented. (For a detailed introduction to gravity and gravity gradiometry please refer to (Torge, 1989) and (Rummel, 1986)).

A point mass which is located at $\mathbf{x}_0 = (x_0, y_0, z_0)$ produces at the measurement location $\mathbf{x} = (x, y, z)$ a disturbing potential

$$T = -\frac{GM}{r}, \quad (1.1)$$

where

$r = \sqrt{(x - x_0)^2 + (y - y_0)^2 + (z - z_0)^2}$ is the distance between \mathbf{x}_0 and \mathbf{x} ,

$G = 6.67428 \cdot 10^{-11} \frac{\text{m}^3}{\text{s}^2\text{kg}}$ is the gravitational constant and

M is the mass of the probe.

We obtain the disturbing acceleration \mathbf{g} by taking the gradient of T

$$\mathbf{g} = \text{grad } T = \begin{pmatrix} T_x \\ T_y \\ T_z \end{pmatrix} = \begin{pmatrix} \partial T / \partial x \\ \partial T / \partial y \\ \partial T / \partial z \end{pmatrix} = \frac{GM}{r^3} \begin{pmatrix} x - x_0 \\ y - y_0 \\ z - z_0 \end{pmatrix}. \quad (1.2)$$

Through a further gradient operation we obtain the disturbing gravity gradient tensor

$$\text{grad } \mathbf{g} = \text{grad}(\text{grad } T) = \begin{pmatrix} \partial^2 T / \partial x^2 & \partial^2 T / \partial x \partial y & \partial^2 T / \partial x \partial z \\ \partial^2 T / \partial y \partial x & \partial^2 T / \partial y^2 & \partial^2 T / \partial y \partial z \\ \partial^2 T / \partial z \partial x & \partial^2 T / \partial z \partial y & \partial^2 T / \partial z^2 \end{pmatrix} = \begin{pmatrix} T_{xx} & T_{xy} & T_{xz} \\ T_{yx} & T_{yy} & T_{yz} \\ T_{zx} & T_{zy} & T_{zz} \end{pmatrix}. \quad (1.3)$$

In this tensor five gradients are independent and four are redundant as follows:

$$\begin{aligned} T_{xy} &= T_{yx}, \\ T_{xz} &= T_{zx}, \\ T_{yz} &= T_{zy}, \\ T_{zz} &= -(T_{xx} + T_{yy}). \end{aligned}$$

Therefore it is sufficient to specify these five independent tensor elements:

$$\begin{aligned} T_{xx} &= \frac{GM}{r^5} (-3(x - x_0)^2 + r^2), \\ T_{xy} &= \frac{GM}{r^5} (-3(x - x_0)(y - y_0)), \\ T_{xz} &= \frac{GM}{r^5} (-3(x - x_0)(z - z_0)), \\ T_{yy} &= \frac{GM}{r^5} (-3(y - y_0)^2 + r^2), \\ T_{yz} &= \frac{GM}{r^5} (-3(y - y_0)(z - z_0)). \end{aligned}$$

As an example a gravity gradient tensor for a single point mass anomaly will be displayed in figure 1.2.

The formula for computing the mass M in the formulas above for an homogeneous sphere or point mass is

$$M = \frac{4}{3} \pi \Delta \rho R^3,$$

with the density contrast $\Delta\rho$ and the radius of the sphere R .

The difference in density is interpreted as

$$\Delta\rho = \rho_s - \rho_a,$$

with the density of the surroundings ρ_s and the density of the anomaly ρ_a .

For the example in figure 1.2 a $\Delta\rho = -300 \text{ kg/m}^3$ is chosen. This is equivalent for the anomaly to consist of basalt ($\rho_a \approx 3000 \text{ kg/m}^3$) and the surroundings to consist of granite ($\rho_s \approx 2700 \text{ kg/m}^3$). The point mass is located 8 km below the origin of the coordinate system. Its radius is chosen to be $R = 5 \text{ km}$.

In figure 1.2 the computed gravity gradient tensor components are displayed.

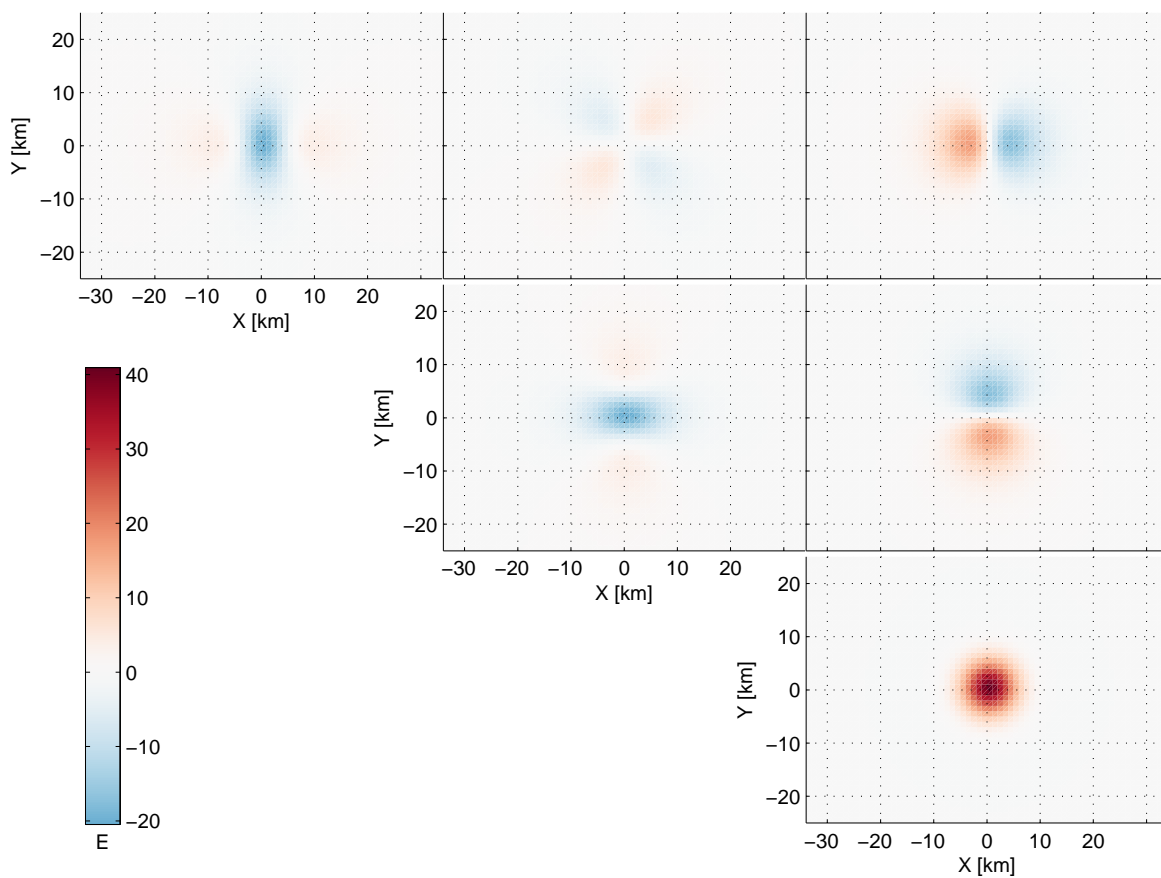


Figure 1.2: Example of the gravity gradient tensor components $T_{i,j}$ of a point mass anomaly.

Chapter 2

Data analysis

It should be noted first that in the original data set two wrongly assigned measuring points occur:

- ending point of “line 47” which should be the first point of “line 48” and
- ending point of “line 59” which should be the first point of “line 60”.

These points are now assigned correctly and are used in the further elaboration.

2.1 Data record

The data record contains *3D Full Tensor Gravity Gradiometry* data acquired by Bell Geospace.

The data were measured with a gravity gradiometer which was installed on a ship. The ship was navigated on lines parallel to an axis in northwest-southeast direction. The hereby gathered data are grouped in so called *lines*. After that the course of the ship was changed. It was then navigated in lines parallel to an axis in northeast-southwest direction crossing the former *lines* at a right angle. To distinguish the hereby gathered data from the ones gathered before these data are grouped in so called *ties*.

It will always be referred to *lines* and *ties* in this emphasised form when there is a need to distinguish between them. In all other cases they will be simply called “lines” (not emphasised).

2.1.1 Measurement area

The surveyed area is located to the North of Scotland midways between Faroe Islands and Shetland Islands (see figure 2.1).

Between these two groups of islands exists a rift called the Faroe-Shetland trough (also known as Faroe-Shetland channel or Faroe-Shetland basin). This rift is up to 1500 m deep and at its smallest 25 km wide.

It is stated by Bell Geospace (2009) and also by Smallwood et al. (2001) that there exist some thick basaltic lava units. Between 1999 and 2002 five surveys were conducted in this area. The examined data record consists of some of these acquired data.

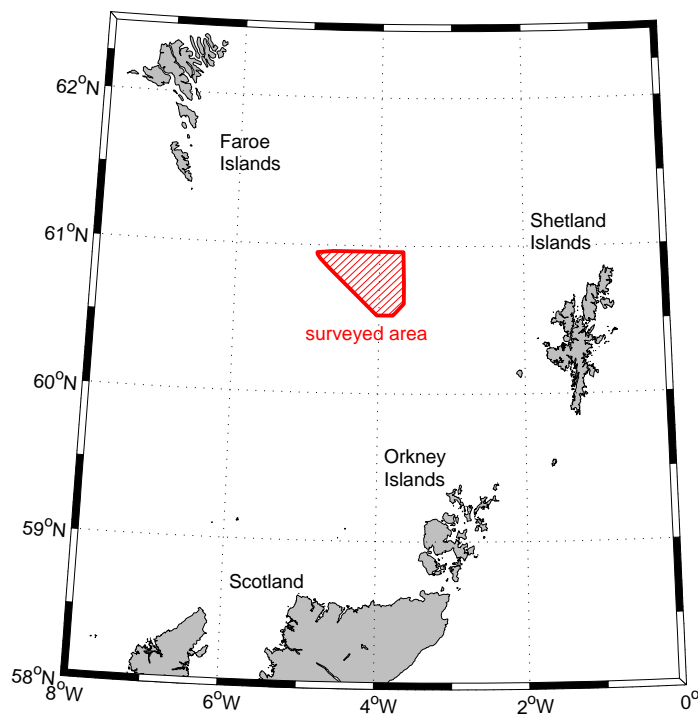


Figure 2.1: The surveyed area between Faroe Islands and Shetland Islands.

The geographical positions of the measuring points are based on the ED 50¹.

Why the ED 50 was chosen as the coordinate system and not one of the newer like ED 77, ED 79 or even WGS 84 or GRS 80 is not known to me. It may be out of historical reasons because some existing maps of this area are based on ED 50. Therefore it is not necessary to compute some coordinate transformations.

The measurement area spreads between 60.53° and 60.96° northern latitude und between 3.66° and 4.87° western longitude.

The cartesian coordinates of the measurement points given in TM 30 (Transverse Mercator, strip 30) are measured by GPS. So it is possible to draw a direct conclusion about the dimensions of the measurement area.

The dimensions are about 48.5 km in north-south direction and about 65.1 km in east-west direction. Altogether the surveyed area spreads over 2068 km².

The bathymetry gives a smooth trough structure without particular visible anomalies which would let us to deduce certain geological formations (see figure 2.2). The depth in the surveyed area is between 517.21 m and 1138.57 m. The average depth is 962.23 m.

2.1.2 Distances

The distances between *lines*, *ties* and measurement points are of further interest.

¹ED 50 – European Datum 1950, based on the International Ellipsoid of 1924 (J. F. Hayford) with semi major axis $a = 6\,378\,388$ m and flattening $f = \frac{a-b}{a} = \frac{1}{297}$, base is the Helmersturm in Potsdam.

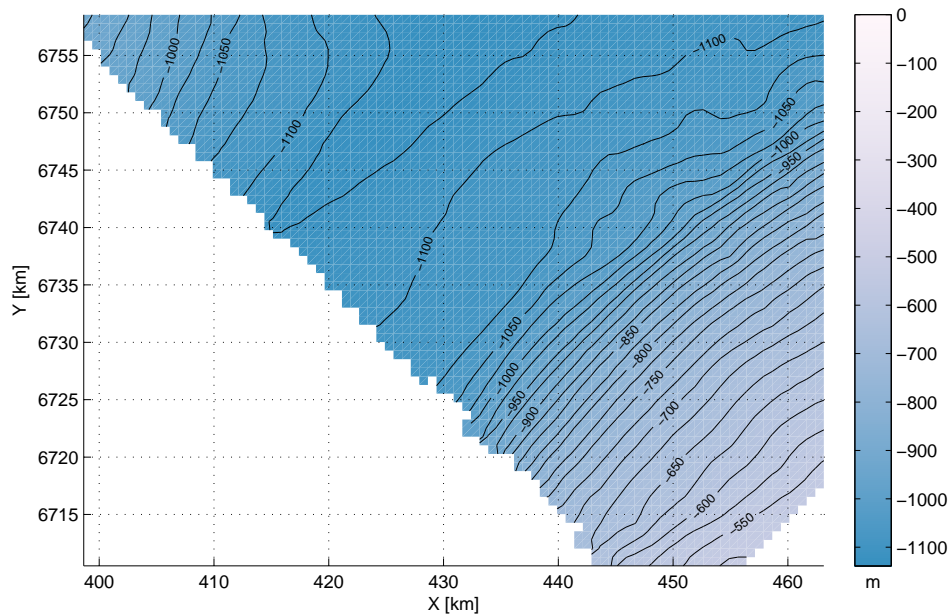


Figure 2.2: Swath bathymetry of the surveyed area which is a part of the Faroe-Shetland trough (between Faroe Islands and Shetland Islands).

The interval between *lines* is 750 m and the interval between *ties* is 2250 m. This regular raster is shown in the NE-corner of figure 2.3. There exist additional diagonals between the *lines* in the dataset which display the same intervals between them as the “normal” *lines*. In an overall view the density of the *lines* is increased. It is inappropriate to give an average distance considering the diagonals. Because of their nature, this computation would be only correct for the middle part of the *lines*.

It was a little tricky to determine the distances of the *lines* automatically. Some of the *lines* were left out and measured afterwards. But the *lines* occur in the dataset in the order they were measured. Hence the distance between lines was only determined for a smaller batch of lines which has no left outs. It seems that the result of this smaller batch is sufficient. So no ordering of the data had to be done manually.

The *ties* were measured in order. Therefore this problem does not apply to them.

Only the absolute difference from the estimated straight line was computed. This is due to the complexity of determination whether the ship yaws portside or starboard. As well we do not need to know this in detail.

The appointed course was held pretty accurate: The mean value of the course deviation is 10.1 m and its standard deviation σ is 17.9 m while the maximum deviation shows a value of 237.0 m. Such a big deviation occurs on some of the diagonal *lines* or in the border areas where the ship turned and therefore did not meet the appointed course. The latter must not concern us further.

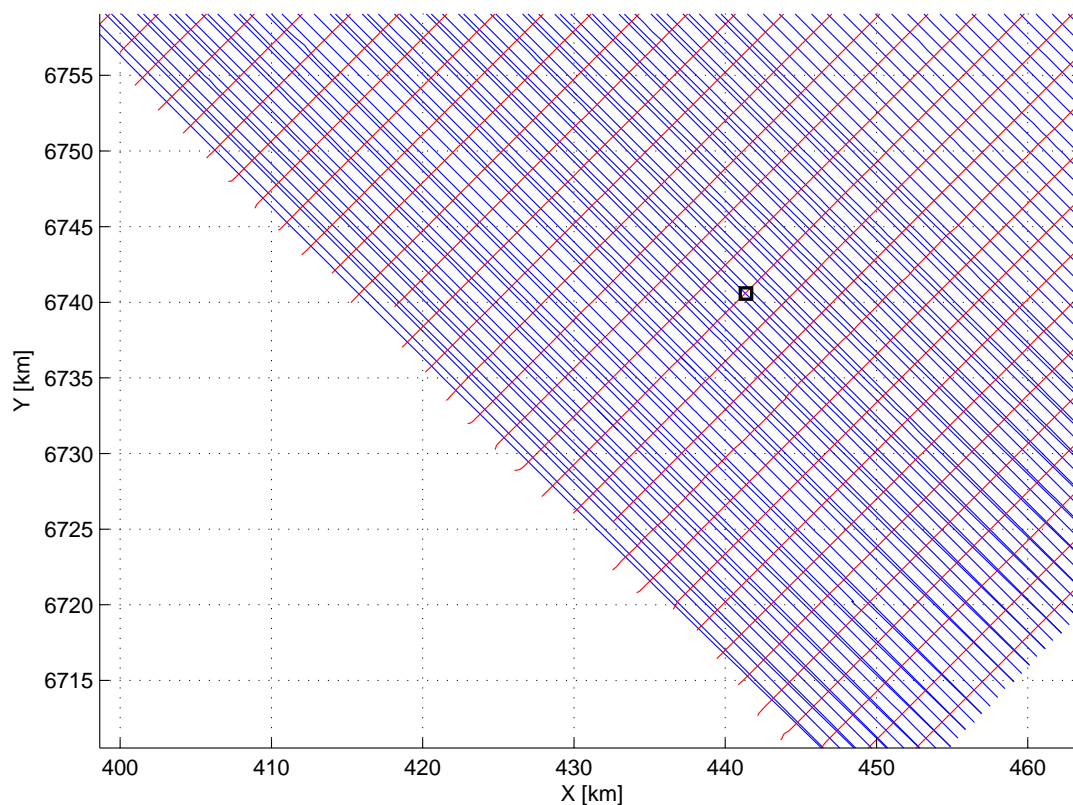


Figure 2.3: Trajectories of the survey. Lines are blue, ties are red. The black box (edge length 750 m) is shown in detail in figure 2.4.

Because deviations only occur on the diagonals numerously, we seek an explanation for this effect. The diagonals were measured later than the rest of the *lines*. So one can conjecture that the ship drifted in the areas with course deviations due to an upcoming wind or an upcoming ocean current (like tidal currents).

In figure 2.5 such course deviations which exceed $3\sigma = 53.7$ m from the appointed course are marked with black dots.

It seems that the aspired interval between measured points on a line is 15 m. This distance was pretty accurately met with a minimum distance between points of 14.895 m, a maximum of 15.013 m and the mean value of 14.998 m. The standard deviation is 0.007 m. A detail of figure 2.3 that shows some of the measurement locations may be found in figure 2.4.

2.2 Description of the data record

The data are given in ASCII format. A sample of the data set can be seen in table 2.1.

The data fields contain the following informations:

X_ED50_TM30: Easting in datum ED50; projection of UTM zone 30 N, units in meters;

Y_ED50_TM30: Northing in datum ED50; projection of UTM zone 30 N, units in meters;

```

/-----3D Marine FTG data and bathymetry from offshore NW Europe.
/
/-----
/
/X_ED50_TM30 Y_ED50_TM30 Lat_ED50 Long_ED50 bathy Txx Txz Tyx Tyy Tyz Tz1 Tze Tzz
/-----
Line 9
463724.57 6759053.98 60.96 -3.67 1104.70 -2.30 2.51 8.47 -3.08 1.23 5.42 -4.94 5.38
463735.16 6759043.36 60.96 -3.67 1104.61 -2.21 2.46 8.14 -3.48 1.19 5.48 -4.93 5.69
463745.36 6759032.36 60.96 -3.67 1104.52 -2.22 2.39 7.78 -3.83 1.08 5.56 -4.93 6.05
463756.23 6759022.05 60.96 -3.67 1104.43 -2.25 2.30 7.44 -4.17 -0.90 5.65 -4.92 6.42
Line 10
462668.54 6759061.79 60.96 -3.69 1106.32 -1.32 5.81 5.17 1.23 5.42 -5.09 0.09
462679.17 6759051.21 60.96 -3.69 1106.30 -1.47 5.91 5.38 1.19 5.48 -5.09 0.27
462689.70 6759040.53 60.96 -3.69 1106.27 -1.62 5.95 5.63 1.08 5.56 -5.12 0.54
462700.19 6759029.81 60.96 -3.69 1106.25 -1.82 5.98 5.93 0.90 5.65 -5.08 0.92
462710.59 6759018.99 60.96 -3.69 1106.22 -2.02 5.94 6.26 0.65 5.74 -5.07 1.37
462721.21 6759008.41 60.96 -3.69 1106.19 -2.24 5.90 6.61 0.37 5.83 -5.09 1.87
462731.77 6758997.75 60.96 -3.69 1106.16 -2.48 5.86 6.97 0.08 5.91 -5.08 2.41
462742.47 6758987.24 60.96 -3.69 1106.12 -2.69 5.80 7.33 -0.24 5.99 -5.07 2.93
462753.02 6758976.58 60.96 -3.69 1106.07 -2.88 5.77 7.66 -0.59 6.04 -5.06 3.47
462763.65 6758966.00 60.96 -3.69 1106.02 -3.11 5.81 7.96 -0.88 6.08 5.05 3.98
462774.10 6758955.24 60.96 -3.69 1105.97 -3.29 5.83 8.20 -1.16 6.10 5.04 4.45
462784.68 6758944.60 60.96 -3.69 1105.92 -3.47 5.96 8.40 -1.36 6.08 5.03 4.83
462795.13 6758933.85 60.96 -3.69 1105.86 3.68 6.20 8.55 -1.54 6.04 5.02 5.22
462805.60 6758923.11 60.96 -3.69 1105.81 -3.87 6.43 8.65 -1.64 5.98 5.01 5.51
462816.24 6758912.54 60.96 -3.69 1105.76 4.08 6.37 8.70 -1.67 5.90 5.01 5.75
462826.76 6758901.84 60.96 -3.69 1105.71 4.25 5.92 8.73 -1.68 5.82 5.00 5.93
462837.37 6758891.23 60.96 -3.69 1105.65 4.44 5.37 8.73 -1.57 5.76 5.00 6.09
462848.01 6758880.66 60.96 -3.69 1105.60 4.65 4.80 8.72 -1.44 5.71 -4.98 6.11
462858.56 6758870.01 60.96 -3.69 1105.55 4.83 4.50 8.71 -1.28 5.69 5.00 6.11
462869.24 6758859.47 60.96 -3.69 1105.49 4.98 4.22 8.69 -1.11 5.71 5.00 6.08
462879.75 6758848.77 60.96 -3.69 1105.43 5.12 3.93 8.69 -0.95 5.77 4.99 6.07
462890.32 6758838.13 60.96 -3.69 1105.38 5.30 3.83 8.69 -0.79 5.89 4.99 6.10
462900.78 6758827.38 60.96 -3.69 1105.32 5.45 3.72 8.68 -0.66 6.05 4.95 6.10
462911.28 6758816.66 60.96 -3.68 1105.27 5.57 3.75 8.68 -0.55 6.25 4.98 6.13
462921.83 6758806.00 60.96 -3.68 1105.21 5.66 3.75 8.66 -0.49 6.50 4.94 6.16
462932.27 6758795.23 60.96 -3.68 1105.15 5.76 3.74 8.65 -0.48 6.77 4.93 6.24
462942.82 6758784.57 60.96 -3.68 1105.09 5.79 3.71 8.62 -0.52 7.07 4.93 6.31
462953.59 6758774.12 60.96 -3.68 1105.03 5.76 3.66 8.58 -0.59 7.36 4.96 6.36
[...]
Tie 51
463756.93 6724858.35 60.66 -3.66 595.69 6.50 0.14 3.25 0.58 16.81 -5.22 -7.08
463746.39 6724847.69 60.66 -3.66 595.67 6.42 0.34 3.08 0.34 16.47 -5.22 -6.76
463735.90 6724836.96 60.66 -3.66 595.65 6.35 0.22 2.88 0.11 16.10 -5.22 -6.46
463725.47 6724826.18 60.66 -3.66 595.63 6.27 0.17 2.67 -0.07 15.73 -5.22 -6.20
463715.03 6724815.41 60.66 -3.66 595.61 6.20 0.17 2.45 -0.26 15.37 -5.22 -5.94
463704.51 6724804.72 60.66 -3.66 595.59 6.13 0.17 2.22 -0.42 15.06 -5.22 -5.71
463693.95 6724794.06 60.66 -3.66 595.57 6.10 0.17 1.98 -0.58 14.79 -5.22 -5.52
463683.43 6724783.37 60.66 -3.66 595.55 6.05 -0.03 1.75 -0.72 14.59 -5.22 -5.33
463672.97 6724772.62 60.66 -3.66 595.53 5.97 0.02 1.52 -0.85 14.46 -5.22 -5.12
463662.45 6724761.93 60.66 -3.66 595.51 5.91 -0.35 1.31 -0.96 14.41 -5.22 -4.95
463651.93 6724751.23 60.66 -3.66 595.48 5.84 1.11 -1.08 -1.08 14.43 -5.22 -4.76
463641.36 6724740.60 60.66 -3.67 595.46 5.72 0.80 -1.12 1.12 14.51 -5.22 -4.59
463630.88 6724729.87 60.66 -3.67 595.43 5.63 -0.85 0.80 -1.17 14.63 -5.22 -4.46

```

Table 2.1: Small sample of the data set.

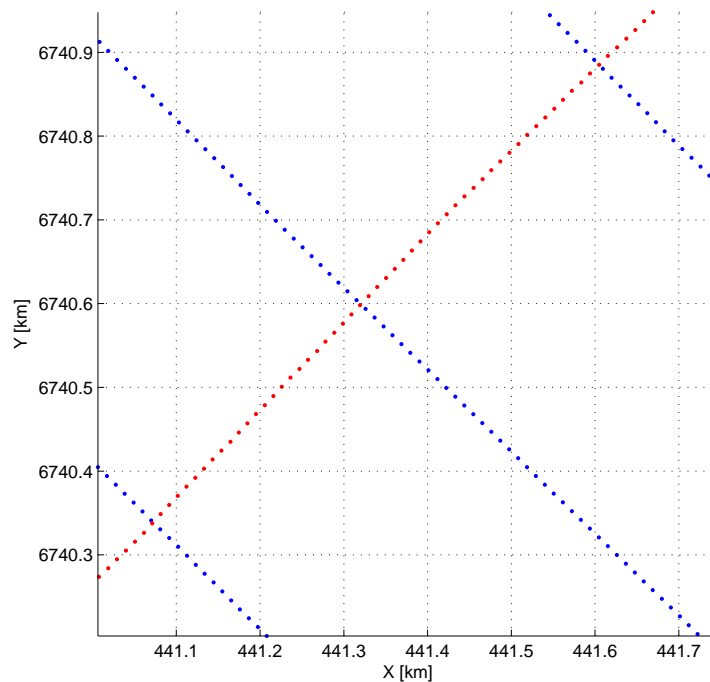


Figure 2.4: Detail of figure 2.3. Lines are blue, ties are red.

Lat_ED50, Long_ED50: Latitude and Longitude in datum ED50, units in decimal degrees;

bathy: Swath bathymetry, units in meters;

Txx, Txz, Tyx, Tyy, Tyz, Tzz: FTG tensor components given in eötvös². The directions of the tensor components are aligned to the cartesian coordinate system mentioned above (though the direction of the z-axis is not clear entirely. Certainly the z-axis runs orthogonally to the x- and y-axis and it seems its direction is towards the mass center of the earth).

Tz1: conventional gravity given in milligal³

Tze: *enhanced gravity* in milligal – this is the conventional gravity integrated with the high frequency component from the FTG data. This gives a gravity measurement with an equivalent spatial resolution of the gradient signature and without influence of host vehicle accelerations (Bell Geospace, 2009).

2.3 Testing of the Laplace equation

Some of the tensor components are redundant, this permits first conclusions about the accuracy of the measurements. As the gradient tensor consists of the second partial derivatives of the potential field, we can make use of Laplace's equation.

²Eötvös: $1 \text{ E} = 10^{-9} \frac{\text{Gal}}{\text{cm}} = 10^{-9} \text{ s}^{-2}$.

³Milligal: $1 \text{ mGal} = 10^{-3} \frac{\text{cm}}{\text{s}^2} = 10^{-5} \frac{\text{m}}{\text{s}^2}$.

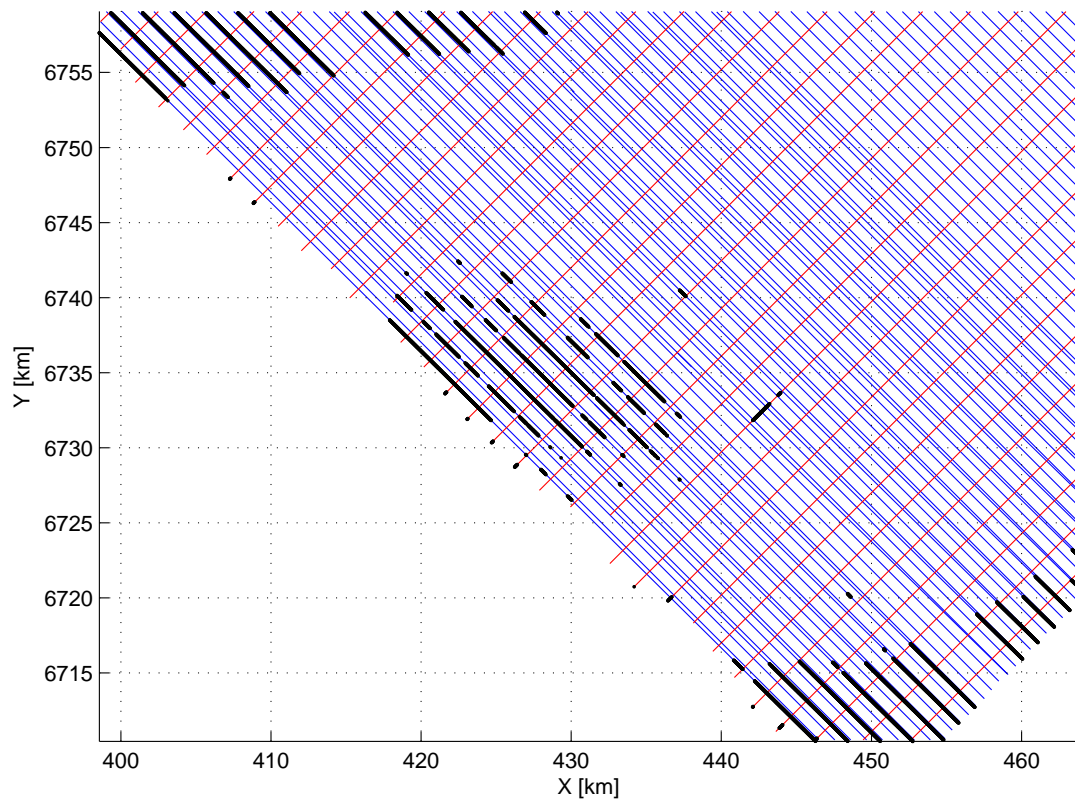


Figure 2.5: Estimated straight lines. Lines are blue, ties are red, course deviations which exceed 3σ from the estimated line are marked with black dots.

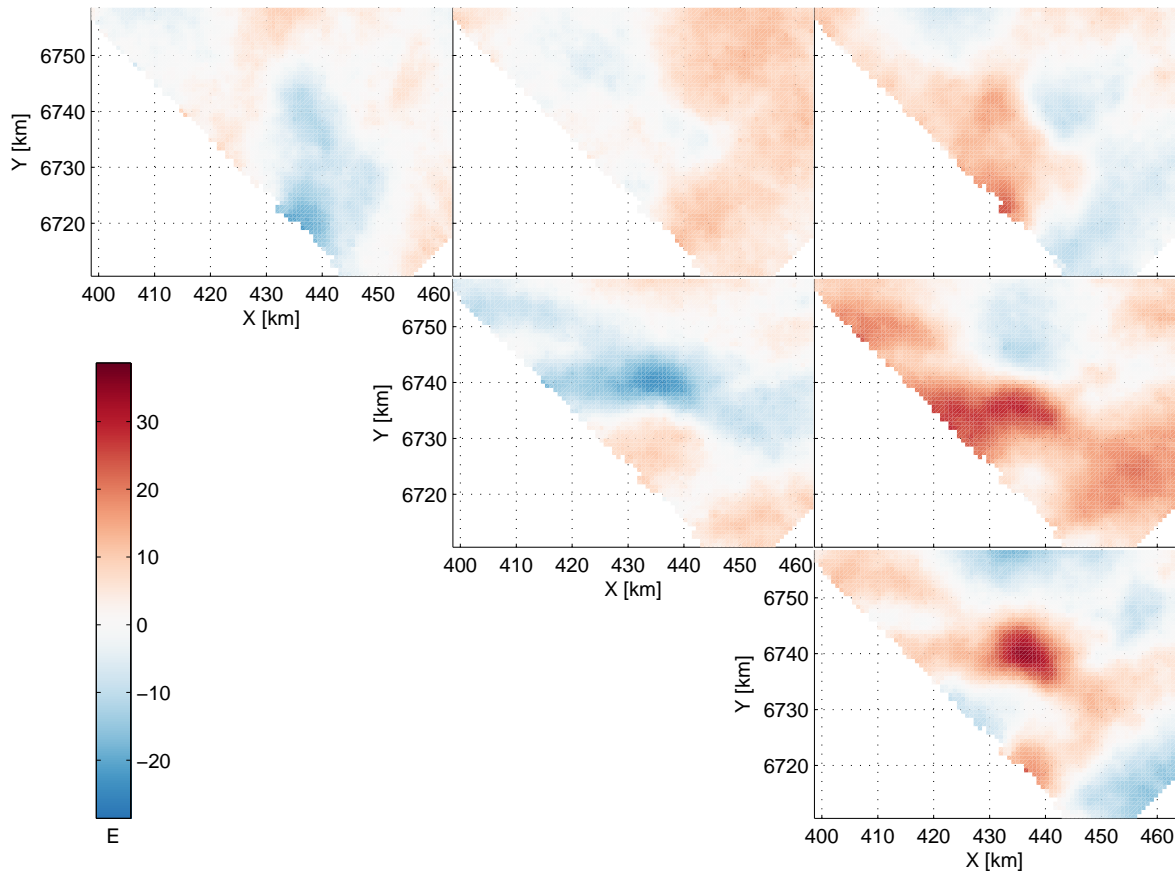


Figure 2.6: Visualization of the tensor components $T_{i,j}$. For this first coarse view the data was interpolated on a raster with an grid size of 750 m.

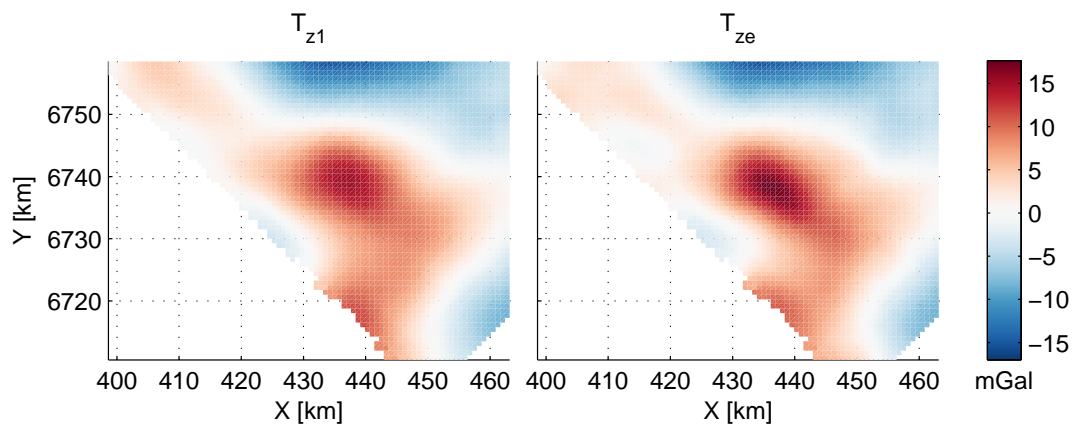


Figure 2.7: On the left side: Conventional gravity T_{z1} ; On the right side: So called enhanced gravity T_{ze} , this is the conventional gravity integrated with the high frequency component from the FTG data.

The Laplace equation for the three dimensional case is

$$\frac{\partial^2 f}{\partial x^2} + \frac{\partial^2 f}{\partial y^2} + \frac{\partial^2 f}{\partial z^2} = 0.$$

Therefore the equation in this case can be written as

$$T_{zz} = -(T_{xx} + T_{yy}), \quad (2.1)$$

which will be analyzed. After reorganisation the equation states that in theory the trace of the gradient tensor must be zero.

$$T_{xx} + T_{yy} + T_{zz} = 0.$$

For the measured tensor data we may assume that a difference to the theoretical value exists. This is caused by measurement errors. All these differences should follow a Gaussian distribution if we imply that no gross errors and no systematic errors were made at measurement time.

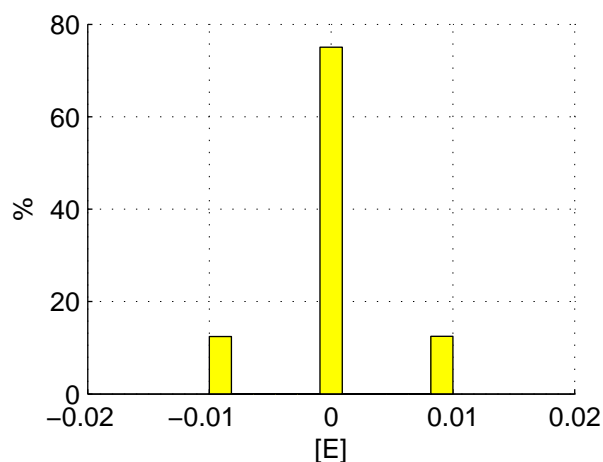


Figure 2.8: Histogram of differences of Laplace's equation $T_{zz} + (T_{xx} + T_{yy}) = 0$

But figure 2.8 shows not the expected Gaussian distribution. There exist only three spikes in the histogram, namely at the values -0.01 E, 0.00 E and 0.01 E.

It seems that at the computation of the gradient tensor data the Laplace equation has been used already. Thus, no independent test on the accuracy of the measurement values is possible, as the Laplace equation is already fulfilled – except for some rounding errors.

2.4 An example – line 53

As an example for the gradient tensor data the trajectory of *line 53* will be shown in figure 2.9. This line was chosen because its course crosses the area of the mass anomaly.

The T_{zz} -component may be considered as the most important component of the gradient tensor because one can get a first impression of the local gravity field easily.

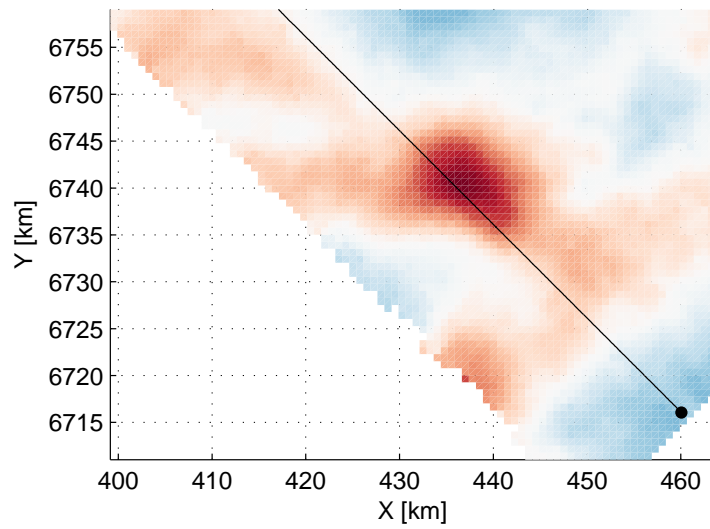


Figure 2.9: Trajectory for line 53. The starting point is marked. As background T_{zz} is displayed.

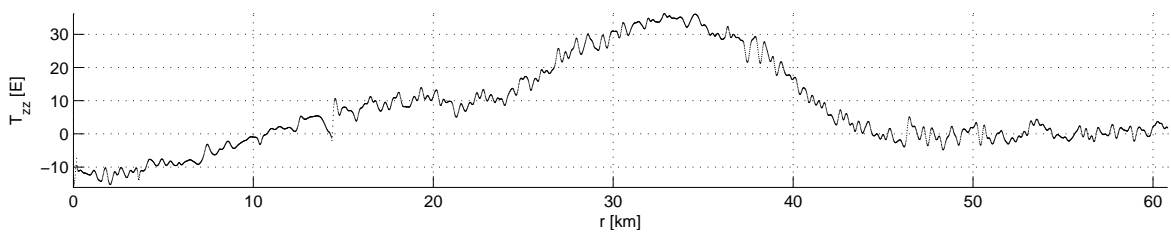


Figure 2.10: T_{zz} of Line 53. The x-axis shows the distance from the starting point.

In figure 2.10 The T_{zz} -component of the gradient tensor is shown. (The graphs of the other components look similar. Therefore they are not visualized).

At a first glance the graph of T_{zz} looks relatively rough. But at a closer look the values follow a (locally) smooth graph. Remember that the measurement locations are 15 m away from each other. So the small oscillations of the signal have a wavelength of about 400–600 m.

Therefore we can assume with a high certainty that this are no local effects of gravity but rather noise.

In the next section we will look into the accuracy of the measurement values. A short look ahead on the results gives away that the measured gradient values contain a big share of noise.

Also Hatch (2004) made an analysis of the noise of an FTG system. But this FTG system was mounted in an aircraft (not on a ship). Hatch mentions a similar noise level as will be found in the next section and some figures denotes a similar wavelength of the noise.

So there is even more evidence that the small oscillations are noise with a relative long wavelength.

Such noise may be recorded due to the rocking motion of the ship in a wavy sea or vibrations caused by the ship's engines. It is possible that the measurement equipment cannot be shielded from such noise completely.

Another explanation could be effects which takes place directly in the gravity gradiometer equipment, e. g. electronic noise which accumulates in the computation of the gradient data (remember that the data are recorded at 128 Hz and processed further, see 1.2.1). But this is only an assumption which is most speculative because no further information on the processing of the data was available.

2.5 Accuracy analysis of the measured data

For the surveyors it is important and interesting to know the accuracy of the measured data. Therefore an accuracy analysis of the data derived by Bell Geospace is presented in the following.

As described, the measured data are given in trajectories which are either called a *line* or a *tie*. Lines and ties intersect at an angle of approximately 90 degrees.

These trajectories are no straight lines because of the ship drifting due to wind or current. Hence it is no trivial act to compute the crossing points of lines and ties.

First we adapt straight lines to the trajectories. From those it is fairly easy to compute the crossing points. But because of the ship's drifting the coordinates of these crossing points are only approximations. To get the "true" crossing point, further steps are necessary.

In a first data analysis we found, that some data gaps appear. Crossing points in such areas can not be evaluated properly. Therefore such "bad" points should be eliminated.

Finding the "true" crossing points and the elimination of "bad" points is possible in one step. We take all measured points on the considered line and tie within an radius of 150 m (this value

seems to be good; because of the ship's drifting the intersection lies within this value in most cases). The distance of measured points is 15 m approximately, therefore we can expect 18 to 20 points to be on a line or tie within this radius. All intersections with less points are considered to be "bad".

There are some intersections where the ship drifted too far from the ideal line, so we get too few points within the specified radius, which means that these points are also eliminated. Fortunately, there are only very few points eliminated. Therefore one does not need to care about them.

If one intersection is marked as "good", we identify the four points which are closest on the line and tie to the "true" point of intersection. This is done with a fast algorithm which tests for intersection. As this algorithm plays only a small role in the analysis it will not be explained here, instead refer to (Sedgewick, 1992) for further information.

Since the trajectories are generally straight, linear interpolation is sufficiently accurate to determine the "true" point of intersection. The outcome of this procedure is visualized in figure 2.11.

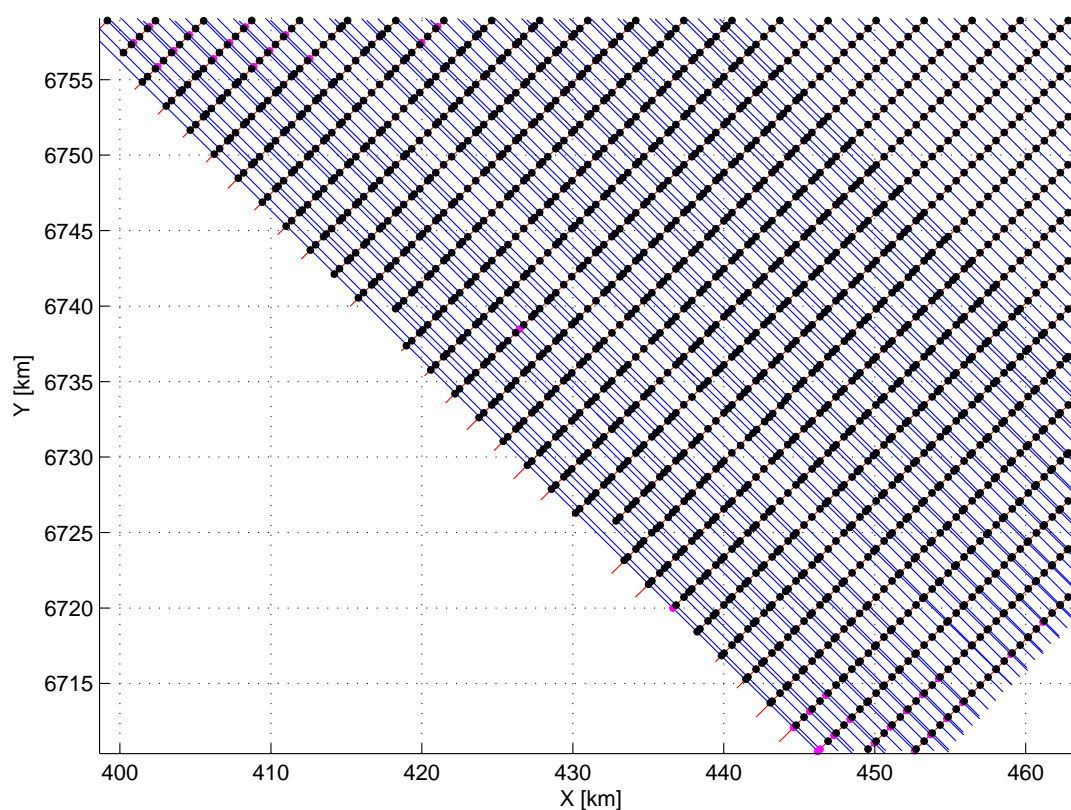


Figure 2.11: Straight lines adapted to the trajectories. The approximated crossing points are marked by dots. A point marked by a magenta colored dot is a "bad" point. This means it is not surrounded by sufficient measure points or the "true" crossing point lies too far away from the crossing point of the adapted lines.

Once one found the "true" crossing points between lines and ties we interpolate the measured data on these points. We do this for lines and ties separately, so that we get two values for each crossing point. One from the data of a line, one from the data of a tie.

Afterwards we subtract the values at the crossing points of the ties from the corresponding values of the lines. Then we do some statistical studies: finding the maximum and minimum values and computing of the mean values and the standard deviation. We will get the values of table 2.2.

	max	min	mean	std
bathy [m]	0.06	-0.10	-0.00	0.01
T_{xx} [E]	9.05	-11.23	0.07	2.22
T_{xz} [E]	2.73	-2.51	0.01	0.23
T_{yx} [E]	7.79	-8.89	0.01	2.22
T_{yy} [E]	8.28	-7.27	-0.11	2.24
T_{yz} [E]	7.47	-8.02	0.01	2.20
T_{z1} [mGal]	0.02	-0.02	0.00	0.00
T_{ze} [mGal]	0.03	-0.03	-0.00	0.01
T_{zz} [E]	7.57	-7.66	0.04	2.29

Table 2.2: Cross-over analysis of measured data: maximum and minimum values at the crossing points and standard deviation between lines and ties.

If we compare these values with the values of table 2.3 we see that the SNR for gravity gradiometry tensor elements is bad with the noise level being about half of the signal. Only T_{xz} seems to be better off with a standard deviation 10 times lower compared to the other tensor elements.

	max	min	mean	RMS
bathy [m]	1138.57	517.21	962.23	979.34
T_{xx} [E]	14.94	-25.80	-0.60	5.37
T_{xz} [E]	25.89	-24.08	1.39	6.62
T_{yx} [E]	18.88	-9.95	4.56	6.70
T_{yy} [E]	22.06	-28.58	-2.01	7.43
T_{yz} [E]	34.93	-18.53	8.21	12.05
T_{z1} [mGal]	15.37	-17.00	1.44	6.39
T_{ze} [mGal]	17.64	-16.80	1.31	6.32
T_{zz} [E]	38.64	-22.30	2.61	9.53

Table 2.3: Analysis of measured data: maximum and minimum values.

The values of T_{z1} and T_{ze} show a good SNR and also have a very small standard deviation. This may be due to the fact that these values were processed. The bathymetric values also have a good SNR and a small standard deviation. The bathymetric data can be measured with high precision.

A listing of minimum, maximum and standard deviation is not very depictive. Therefore the deviation of differences between the line-point and the tie-point will be visualized in histograms. The histograms of the individual tensor components are shown in figure 2.12.

We get the expected picture. Dimensions with small standard deviation have a narrower histogram (T_{xz}). The other histograms are wider accordingly. Why T_{xz} is measured so much better could not be clarified though.

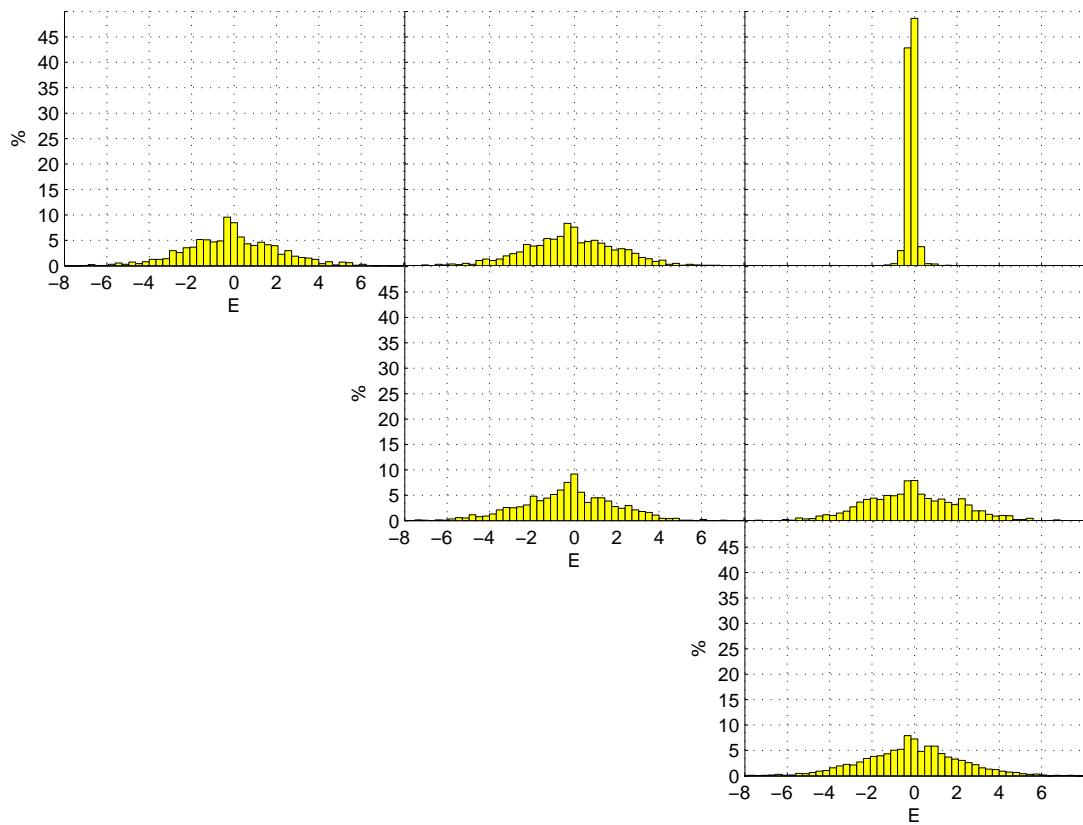


Figure 2.12: Histograms of the differences of tensor components between the line-point and the tie-point.

However, a consideration of the individual components is not sufficient because combined components are used for further analysis. Therefore we should consider the combined tensor components. This is a multidimensional problem, so it is not possible to display it clearly. Hence we consider the combined components as a vector and compute the norm of it. Because we could compute an Euler deconvolution with the components of each line of the tensor, we will consider the vectors $T_{x,i} = (T_{xx}, T_{xy}, T_{xz})$, $T_{y,i} = (T_{yx}, T_{yy}, T_{yz})$ and $T_{z,i} = (T_{zx}, T_{zy}, T_{zz})$ and one vector $T_{i,j}$ containing all independent tensor components. Therefore we compute the Euclidean distances between the vectors on a line and tie in the crossing points, e. g.

$$\|\Delta T_{x,i}\| = \sqrt{\Delta T_{xx}^2 + \Delta T_{xy}^2 + \Delta T_{xz}^2}.$$

The histogram is shown in figure 2.13.

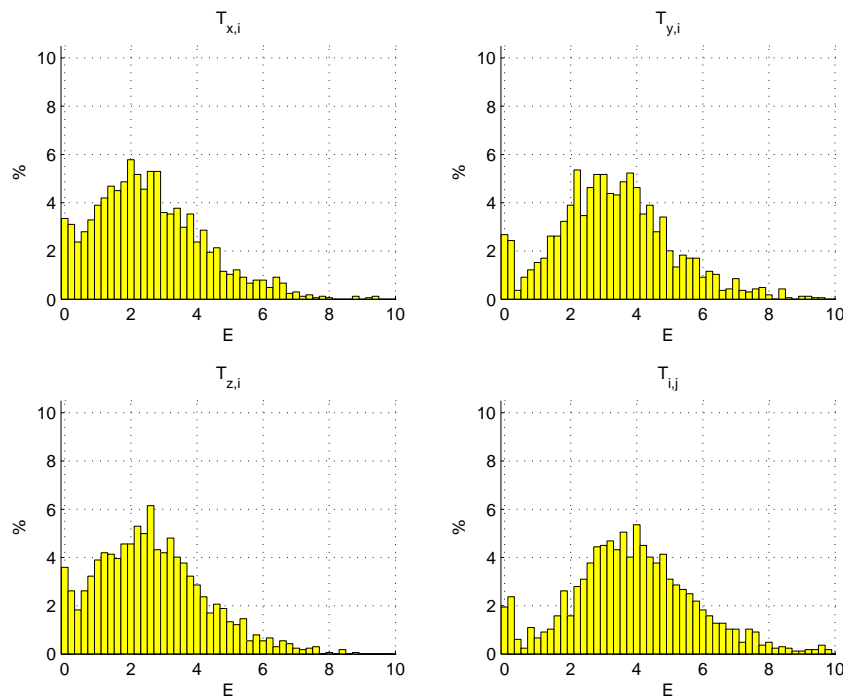


Figure 2.13: Histograms of the differences of combined tensor components between the line-point and the tie-point. E. g. top left is the histogram of $\sqrt{\Delta T_{xx}^2 + \Delta T_{xy}^2 + \Delta T_{xz}^2}$.

2.5.1 Smoothed data

The data seem to be a little rough. Therefore an attempt was made whether by smoothing the data we could get rid of some measurement noise.

The smoothing of the data will be done by a low pass filter. One possible way is to compute the Discrete Fourier Transform (DFT). An efficient algorithm to compute the DFT is given by the Fast Fourier Transform (FFT), which is already implemented in MATLAB.

The Fourier Transform splits a signal in its frequency components. To achieve the low pass filtering, higher frequencies can be cut off by setting them to zero. Afterwards the Inverse

Fourier Transform puts the filtered signal together containing only the remaining frequency components.

In this case a threshold frequency with an index of 10 seems to be well suited. This threshold frequency must be seen in regard to the length of a sample line, as the FFT splits the signal in n frequencies for n given sample points. The outcome may be viewed in figure 2.14.

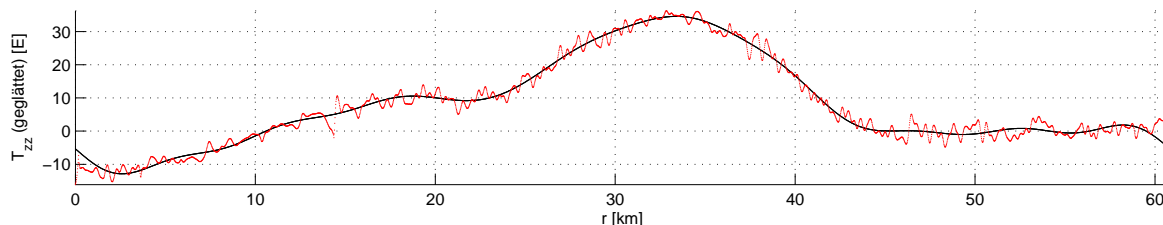


Figure 2.14: Smoothed T_{zz} of Line 53. The x-axis shows the distance from the starting point.

The smoothing by FFT, cutting off high frequencies and IFFT has the flaw that it tends to overshoot. This is also the case on both margins in figure 2.14.

If we compare the values of table 2.4 with the values of table 2.2 we got previously, we see that the smoothing of the data gives slightly better results. The previous outstanding T_{xz} now is comparable with the other values.

	max	min	mean	std
bathy [m]	0.06	-0.10	-0.00	0.01
T_{xx} [E]	6.22	-6.55	0.03	1.34
T_{zz} [E]	6.36	-7.06	0.13	1.26
T_{yx} [E]	4.96	-5.42	-0.01	1.31
T_{yy} [E]	7.94	-7.28	-0.07	1.33
T_{yz} [E]	6.06	-10.36	-0.05	1.49
T_{z1} [mGal]	0.02	-0.02	0.00	0.00
T_{ze} [mGal]	0.03	-0.03	-0.00	0.01
T_{zz} [E]	10.77	-11.53	0.04	1.54

Table 2.4: Cross-over analysis of smoothed data at the crossing points.

We can see this also visualized in figure 2.15.

Also the combined tensor components as shown in figure 2.16 are a better than before.

There exist other methods to smooth the data (e. g. the moving average) which may be better suited.

It has to be tested whether a smoothed dataset will give off better results at Euler deconvolution.

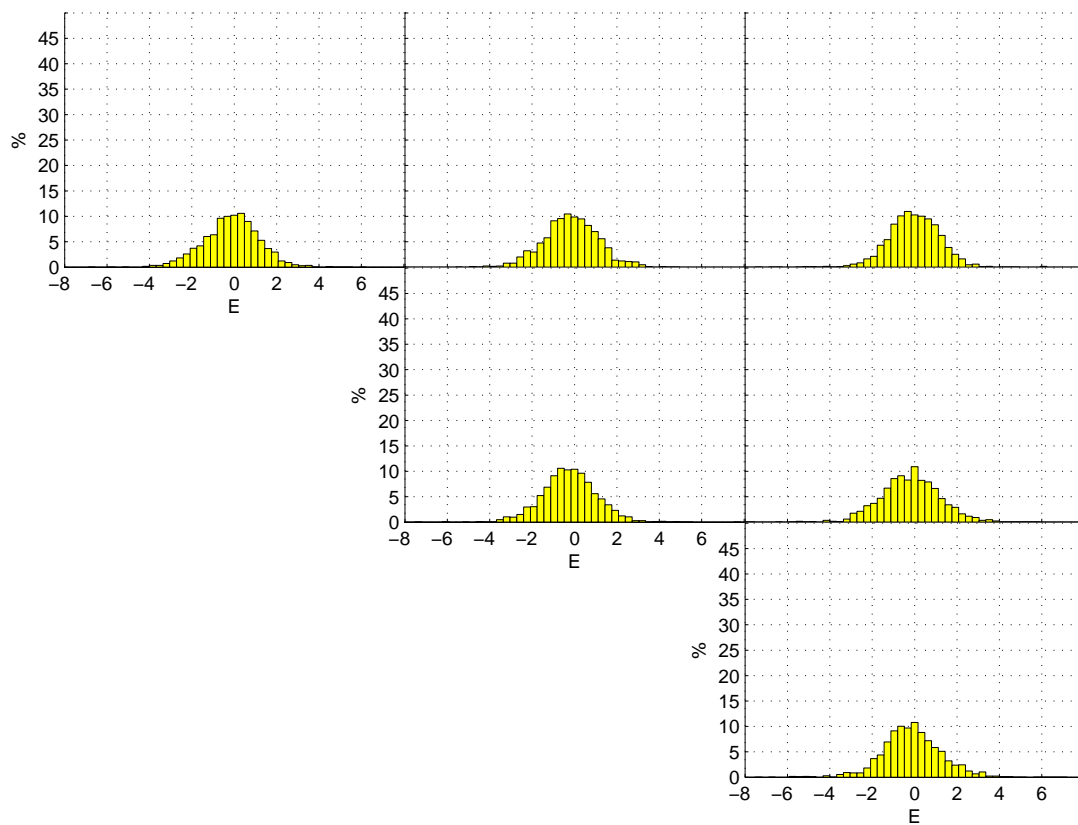


Figure 2.15: Histograms of the differences of the smoothed tensor components between the line-point and the tie-point.

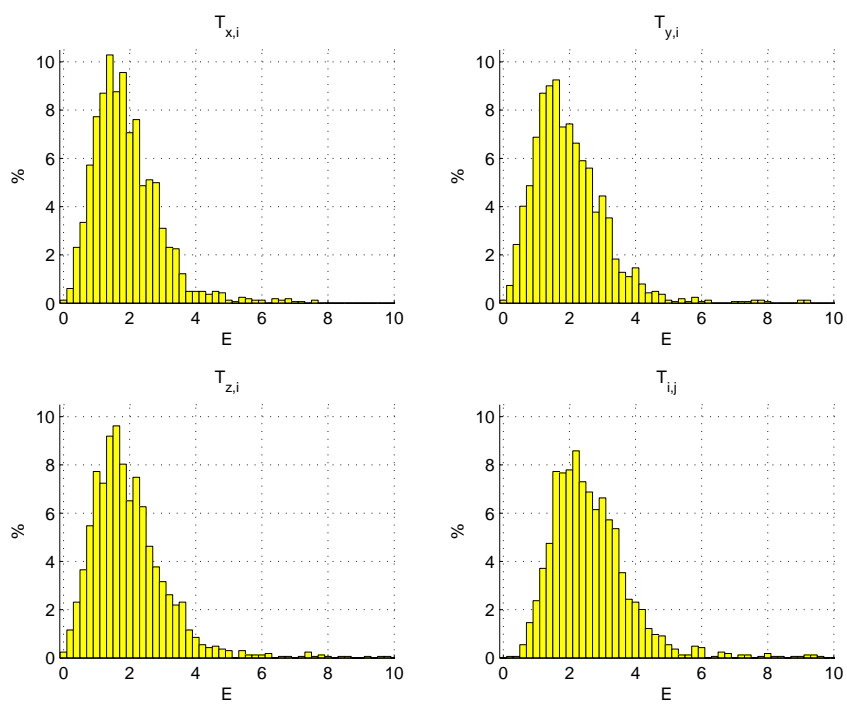


Figure 2.16: Histograms of the differences of combined smoothed tensor components between the line-point and the tie-point.

Chapter 3

Euler deconvolution

3.1 Theory

The Euler deconvolution is a technique to locate the sources of magnetic or gravity anomalies. Its strategy is to consider such anomalies to be caused by many rather simple sources. Such a strategy is useful especially for large data sets with many anomalies in the measurement area, such as long profiles or large areal surveys.

The general form of Euler's equation is given by

$$\mathbf{r} \cdot \nabla f = -nf. \quad (3.1)$$

Functions f that satisfy Euler's equation are said to be homogeneous with degree n .

As any spatial derivative of a homogeneous function is also homogeneous, e. g. taking the partial derivative of (3.1) with respect to z yields

$$\begin{aligned} \frac{\partial}{\partial z} [\mathbf{r} \cdot \nabla f] &= \frac{\partial}{\partial z} f + \mathbf{r} \cdot \nabla \frac{\partial}{\partial z} f \\ &= -n \frac{\partial}{\partial z} f. \end{aligned}$$

which further yields

$$\begin{aligned} \mathbf{r} \cdot \nabla \left[\frac{\partial}{\partial z} f \right] &= \mathbf{r} \cdot \nabla \frac{\partial}{\partial z} f = -n \frac{\partial}{\partial z} f - \frac{\partial}{\partial z} f \\ &= -(n+1) \frac{\partial}{\partial z} f \end{aligned}$$

and in consequence $\frac{\partial}{\partial z} f$ is homogeneous with degree $n+1$ (Blakely, 1995).

For example the function $f = \frac{1}{r}$ (with $r = \sqrt{(x-x_0)^2 + (y-y_0)^2 + (z-z_0)^2}$) satisfies Euler's equation with degree $n=1$. Therefore the gravitational potential of a point mass $f = V = -\frac{Gm}{r}$ also satisfies Euler's equation with the same degree. Analogous, the potential field of other geometries contains higher derivatives of f , thus Euler's equation is satisfied with another value for n (Blakely, 1995).

Hence the degree n is a measure of the rate of change (or fall-off rate) with increasing distance to a source, it is possible to gain information about the structure of the source. Therefore n is also referred to as *structural index* (SI). In table 3.1 some possible values with their meanings for a gravitational field are given.

n	Type of body
0.0	sill / dyke / step
0.5	ribbon
1.0	line of mass (pipe, cylinder of uniform density)
2.0	point mass (sphere of uniform density)

Table 3.1: Structural indices for usage with gravity gradiometry data (Blakely, 1995).

A more commonly used form of Euler's equation (3.1) which is also easier to understand is given by

$$(x - x_0) \frac{\partial f}{\partial x} + (y - y_0) \frac{\partial f}{\partial y} + (z - z_0) \frac{\partial f}{\partial z} = -nf \quad (3.2)$$

where (x_0, y_0, z_0) is the location of the source, (x, y, z) the location of the measurement, n the degree and f the field (Wu, 2007).

To compute the Euler devonvolution a little trick is necessary. We assume that the field f is the sum of a constant base field B and the difference Δf to the actual field:

$$f = \Delta f + B.$$

We also benefit from the fact that (because of $B = \text{const.}$) the following holds:

$$\frac{\partial}{\partial z} (\Delta f + B) = \frac{\partial}{\partial z} \Delta f = \frac{\partial}{\partial z} f.$$

With this equation 3.2 changes slightly:

$$(x - x_0) \frac{\partial \Delta f}{\partial x} + (y - y_0) \frac{\partial \Delta f}{\partial y} + (z - z_0) \frac{\partial \Delta f}{\partial z} = -n(\Delta f + B). \quad (3.3)$$

3.2 Arranging Euler's equation for gravity gradiometry data

The formula 3.2 is fulfilled by the formulas of section 1.3. Please note that we write “ n ” and not “ $(n + 1)$ ” as the spatial derivative of Euler's equation may indicate (see section 3.1). The structural index must be chosen and therefore the “+1” is already considered in table 3.1. So we can set $f = T_z$ and $\frac{\partial \Delta f}{\partial x} = T_{xz}$, $\frac{\partial \Delta f}{\partial y} = T_{yz}$ etc.:

$$(x - x_0)T_{xz} + (y - y_0)T_{yz} + (z - z_0)T_{zz} = -n(\Delta T_z + B_z). \quad (3.4)$$

The same can also be done for the other components of the gravity vector. This yields

$$\begin{aligned} (x - x_0)T_{xy} + (y - y_0)T_{yy} + (z - z_0)T_{zy} &= -n(\Delta T_y + B_y) \\ \text{and } (x - x_0)T_{xx} + (y - y_0)T_{yx} + (z - z_0)T_{zx} &= -n(\Delta T_x + B_x). \end{aligned}$$

So one could use the complete gravity gradient tensor to determine the source of the gravity anomaly.

But we will use only equation 3.4 because in the given data set only the T_z -component of the gravity vector is available (though it should be possible to estimate the missing quantities).

As we have four unknowns in the Euler's equation and we know of the measurement errors, a solution is to be found by an overdetermined parameter estimation. For N sample points the equation 3.4 is reformed to

$$\begin{pmatrix} T_{xx,1} & T_{yz,1} & T_{xz,1} & -n \\ & & \vdots & \\ T_{xx,N} & T_{yz,N} & T_{xz,N} & -n \end{pmatrix} \begin{pmatrix} x_0 \\ y_0 \\ z_0 \\ B_z \end{pmatrix} = \begin{pmatrix} xT_{xz,1} + yT_{yz,1} + zT_{zz,1} + nT_{z,1} \\ \vdots \\ xT_{xz,N} + yT_{yz,N} + zT_{zz,N} + nT_{z,N} \end{pmatrix} \quad (3.5)$$

(see also Mushayandebvu et al. (2004)).

The usual practice is to slide a window of size N over the profile or the raster data of a survey area. Usually for raster data the window is quadratic while for profile data the window is linear.

For each position of the window one estimate of the source's location is computed. These estimates tend to cluster in zones of magnetisation or density contrasts of geologic interest (Blakely, 1995).

The window size should be chosen to be large enough that the gravitational effect of a single source is covered but it should be small enough that significant effects from multiple sources are not included (Wu, 2007).

Now the equation 3.5 is of the form

$$\mathbf{Ax} = \mathbf{y}.$$

The Euler deconvolution is achieved with a standard least squares parameter estimation:

$$\mathbf{y} = \mathbf{Ax} + \mathbf{e} \quad \implies \quad \mathbf{A}^T \mathbf{y} = \mathbf{A}^T \mathbf{Ax} \quad \implies \quad \hat{\mathbf{x}} = (\mathbf{A}^T \mathbf{A})^{-1} \mathbf{A}^T \mathbf{y}$$

with the vector of "observations" \mathbf{y} being the right hand side of equation 3.5, the design matrix \mathbf{A} and the vector of parameters \mathbf{x} or rather $\hat{\mathbf{x}}$.

However in some cases (mostly error-free test cases) the numerical computation fails because the inverse of $\mathbf{A}^T \mathbf{A}$ becomes near singular. This is due to the small gravity gradient values in comparison with the value of n . One can avoid this problem if one uses the singular value decomposition.

Any $m \times n$ matrix \mathbf{X} can be decomposed to

$$\mathbf{X} = \mathbf{U} \mathbf{S} \mathbf{V}^T.$$

where

- \mathbf{U} is a $m \times m$ orthogonal matrix,
- \mathbf{S} is a $m \times n$ matrix of "diagonal type", i. e. $s_{ij} = 0$ for $i \neq j$ and
- \mathbf{V} is a $n \times n$ orthogonal matrix.

\mathbf{X}^+ is called the pseudoinverse of \mathbf{X} and is given with

$$\mathbf{X}^+ = \mathbf{V} \mathbf{S}^+ \mathbf{U}^T$$

where \mathbf{S}^+ is a $n \times m$ matrix of “diagonal type” with the elements $s_{ii}^+ = 1/s_{ii}$ für $s_{ii} \neq 0$ (Råde and Westergren, 1995).

The Moore-Penrose pseudoinverse uses the singular value decomposition and provides a numeric robust least squares solution to a system of linear equations. Such a function is implemented in MATLAB already. With this we got a second way to compute the parameters:

$$\mathbf{y} = \mathbf{A}\mathbf{x} \quad \Longrightarrow \quad \hat{\mathbf{x}} = \mathbf{A}^+\mathbf{y}.$$

3.3 Testing of the Euler Deconvolution

The Euler Deconvolution will be tested theoretically with simulated error free gradient data in 2D. Because of the data being generated we know the centers of the causative mass anomalies and also their sizes. Therefore it is possible to verify the functionality of the Euler Deconvolution.

Later we add noise to the simulated data. This added noise is similar to the noise of the real data in its amount and wavelength.

We also perform an Euler Deconvolution with the noisy simulated data. Thus we can analyse whether the noise disturbs the Euler Deconvolution and in which amount.

3.3.1 Determination of the centers of mass anomalies

As mentioned before Euler Deconvolution uses a sliding window to determine its solutions. We get a huge vector of solutions which are coordinates of mass centers. But not all of these coordinates give a proper mass center. So we need to find a way to extract possible mass centers out of this huge vector.

Solutions of the Euler Deconvolution tend to lump if an actual mass center exists. Actually I use two simple methods to gather the solutions to determine possible mass centers.

Raster This method is a simple one: Gather all solutions which fall into a raster cell. Color this cell according to the number of gathered solutions.

One major problem emerges if solutions are lumping around a borderline between raster cells. If this is the case, the neighboring cells gather similar amounts of solutions. Thus resulting in splitting the importance of this mass center. So it may be overseen.

Sum of reciprocal distances This method tries to overcome the disadvantage of the raster gathering.

We compute the sum of all reciprocal distances from one point j to all of the other points

$$d_j = \sum_{i=1}^N \frac{1}{|\mathbf{x}_i - \mathbf{x}_j|^{1/2}}, \quad \text{with } N = \text{number of all points.}$$

Together these single sums d_j build the vector \mathbf{d} .

The reciprocal sum is bigger for a point within the neighbourhood of other points and smaller for more isolated points.

For finding possible solutions of the Euler Deconvolution all points which get a reciprocal sum $d_j < \bar{d}$ (where \bar{d} is the median of all values of \mathbf{d}) is considered a false positive and will be removed. In most cases multiple points of the clustered solutions meet the criterion to remain. So there will be multiple solutions displayed which overlap each other. The radius of a displayed circle corresponds to its reciprocal sum.

At first a multiple of the standard deviation of \mathbf{d} was considered but the median seems to work better without trying too much.

3.3.2 Euler 2D

In a 2D-case equation 3.4 can be simplified considerably because of $y = y_0 = 0$:

$$(x - x_0)T_{zx} + (z - z_0)T_{zz} = -n(\Delta T_z + B_z).$$

After reorganisation for known terms and unknown terms like before we get the observation equation

$$xT_{zx} + yT_{zz} - n\Delta T_z = x_0T_{zx} + y_0T_{zz} - nB_z.$$

Euler's equation is fulfilled for gravity gradiometry data by the structural index $n = 2$ for a point mass. So on the left hand side of this equation no more unknown terms occur.

The fictitious testing line will be 5 km long.

We compute the needed values of T_{zx} , T_{zz} and T_z beforehand (see the two graphs at the top of the figures in section 3.5). Therefore we assume center and radius of one or more mass anomalies. For a better visualization the probes will be shown as green ellipses (not circles as the scalefactors for both axes are not the same) in the graph in the middle of these figures.

For the noiseless case here tested the size of the sliding window is set to 12 samples.

Single point mass For the simplest case a point mass is chosen which is set at a defined location $\mathbf{x}_0 = (x_0, z_0)$ and produces at location $\mathbf{x} = (x, z)$ a disturbing potential T (for formulas see section 1.3).

We examine the generated trajectory of simulated measurement points. The probe lies near the center of the line in a depth of 300 m and its radius is $r_M = 75$ m.

At the first try the probe has a density contrast of $\Delta\rho = -300 \frac{\text{kg}}{\text{m}^3}$. This is comparable to basalt ($\rho \approx 3000 \text{ kg/m}^3$) surrounded by granite ($\rho = 2700 \text{ kg/m}^3$).

At the second try we will have the same scenario. But we swich basalt and granite so that the granite probe is now surrounded by basalt. Hence the difference in density is $\Delta\rho = +300 \frac{\text{kg}}{\text{m}^3}$.

With these values we compute the Euler Deconvolution.

In the figures 3.2 and 3.3 the outcome is visualized. Although $\Delta\rho$ is positive in the first case and negative in the second case the outcome of the Euler Deconvolution is the same.

To prevent questions it should be mentioned that due to the Moore-Penrose pseudoinverse some wrong solutions of the Euler Deconvolution are introduced. This is a numerical problem and is visible in both of the figures in the middle graph: Not all of the solutions lie in the point in the middle of the point mass. Also it is only visible in the ideal case with one point mass present.

Multiple point masses The figures 3.4 to 3.9 show the outcome of the Euler Deconvolution for multiple point masses.

Conclusion An examination of the figures 3.2 to 3.9 shows that generally speaking the Euler Deconvolution is functioning. It also shows us some minor flaws of the Euler Deconvolution:

- The solutions tend to “loop” around a mass center. Sometimes the loop has a wider hole, sometimes the hole is smaller. The size of the loophole has a direkt effect on both of the used methods to extract the position of the mass center. The bigger the hole, the smaller the result, i. e. the smaller the printed circle in the figure.
- There are false positives or “ghost masses” present (e. g. figures 3.6, 3.7 and 3.9). So we may think about an even better threshold criterion (though not done here).
- The more distinct the masses, the more distinct the outcome of Euler Deconvolution. Masses lumped together as in figure 3.8 can not be distinguished properly.

3.3.3 Euler 2D – added noise

All measured gravity gradient data contain also a significant level of noise. As seen before the noise is not a random component on each measurement point but has a longer wavelength.

In this section we will see how the window size influences the Euler Deconvolution on noisy data. The noise will be at a level of 10% of the actual maximum of the signal of the gravity gradient components T_{xz} and T_{yz} . The signal of T_z will remain untouched as it is also smooth in the data set of Bell Geospace.

Size of the window We will only examine a test series (figures 3.10 to 3.12) in which one mass probe is present.

On the noise free test series a window size of 21 samples was used. In this test series we started with a window size of also 21 samples and doubled this size for each new Euler Deconvolution.

As we see in the figures this time a window this small is of no use. Until the window size reached 641 samples the Euler Deconvolution is of no use at all because of the noise. (Therefore figures with smaller window sizes are not shown). From here on we see an advancement with each doubling of the window size.

The peak of the mass probe's influence on the gravity field starts at 2000 m and ends at 3000 m roughly. The conclusion is that the window size needs to be about the size of the main influence of the probe on the gravity field data to compute the Euler Deconvolution successfully.

Depth and size of the probe mass This test series (figures 3.13 to 3.15) looks upon the behaviour of the Euler Deconvolution dependent on depth and size of the probe mass.

We have five bodys whose locations descend.

The first case is without noise and Euler Deconvolution detects the locations of the bodys without bigger problems (only some "ghost masses" remain).

The second case has the same scenario but noise added on the signal. Here only the first two bodys are detected. As the gravity signal broadens and gets shallower with depth the rest of the bodys disappears behind the noise.

The third case is as the second but the bodys get larger with depth. Now Euler Deconvolution detects the bodys without greater problems apart from the "ghost masses" which appear due to the noise.

Influence of noise In figures 3.16 to 3.19 the influence of different noise on the same bodys is tested.

The first and second figure contains different noise at 10% of the signal. The third and fourth figure contains the same noise as the first figure but at 20% and 30%.

Different noise at the same level has no significant influence in the outcome.

Like before the deeper the mass located the more the Euler Deconvolution is disturbed by noise all the more if the noise level is rising.

Structural index In figures 3.20 to 3.23 different values for the structural index n are tested.

We test values of $n = 0.5$ (because with $n = 0$ the designmatrix is singular), $n = 1$, the correct value for point masses $n = 2$ and $n = 3$.

As we can see the mass body is the better located the better n fulfils the Euler's equation.

3.4 Euler deconvolution with real data

Some trajectories of the gravity gradiometry data set were chosen: *line 53* from before and its neighbour *line 54*, *line 65* and *tie 40*.

Figure 3.1 shows their locations.

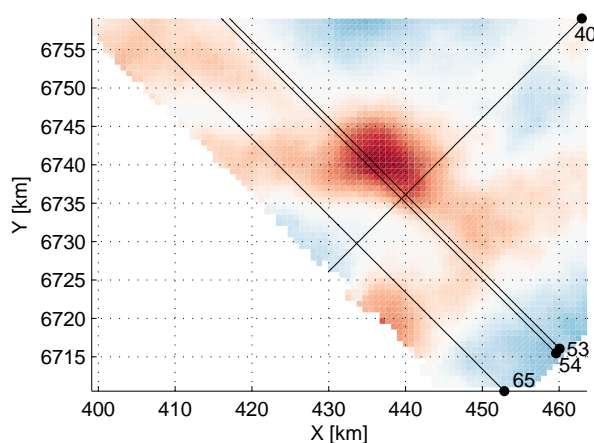


Figure 3.1: Chosen trajectories for Euler deconvolution.

3.4.1 Raw data

In figures 3.24 to 3.27 the Euler deconvolution was done with the gravity gradient data set.

Now the sample distance is 15 m. Hence the window size was chosen to be 1001 samples. This is due to the size of the gravity anomaly which should be detected. Euler deconvolution with smaller window sizes was tried but gave no reasonable result. Bigger window sizes tend to “overlook” smaller structures.

The figures are like before. The scale of the y-axis is now chosen by MATLAB automatically because the Euler deconvolution gives with the raw data also results which are clearly false. Especially this is the case in figure 3.27 where all solutions are above sea level.

The two neighbouring lines create similar results (apart from some “ghost masses”): the locations near 12 km and near 25 km are nearly the same for both lines.

3.4.2 Smoothed data

In figures 3.28 to 3.31 the Euler deconvolution was repeated with smoothed data. All other parameters are the same like before.

If one compares the figures of the smoothed data to the figures of the raw data, one can see that the outcome is a little better: there appear fewer “ghost masses.”

Because of the big sliding window which was used for the estimation of the location of the source, the raw data get a similar smoothing by the process.

Also for *tie 40* the result did not get better. It seems that this trajectory is too short to cover the mass anomaly in whole and therefore the Euler deconvolution can not handle the data properly.

3.5 Figures of the Euler deconvolution

In this section all the figures of the test cases of the Euler deconvolution are gathered.

Each figure displays in the graph to the top the gravity vector component T_z (blue). Also the window size (red) is shown. The sample distance in the real data set is different to the synthetic data. With this one can get a visual impression of the connection between the influence of the mass body on the gravity data and the window size (which is similar to the number of samples used for the estimation).

The graph second to the top displays the gravity gradient tensor components T_{xz} and T_{zz} (black and red).

The graph in the middle of the figures displays the location of the probe and the space which it occupies (green). Also all solutions of the Euler deconvolution (blue) are shown.

The graph second to the bottom displays the solutions gathered in a raster. The darker a raster cell the more solutions it contains.

The graph at the bottom shows the result of the reciprocal sum. The bigger a circle the bigger the value of the sum. The circles indicate the places where the solutions of the Euler deconvolution cluster.

For further explanations of the figures please refer to page 32.

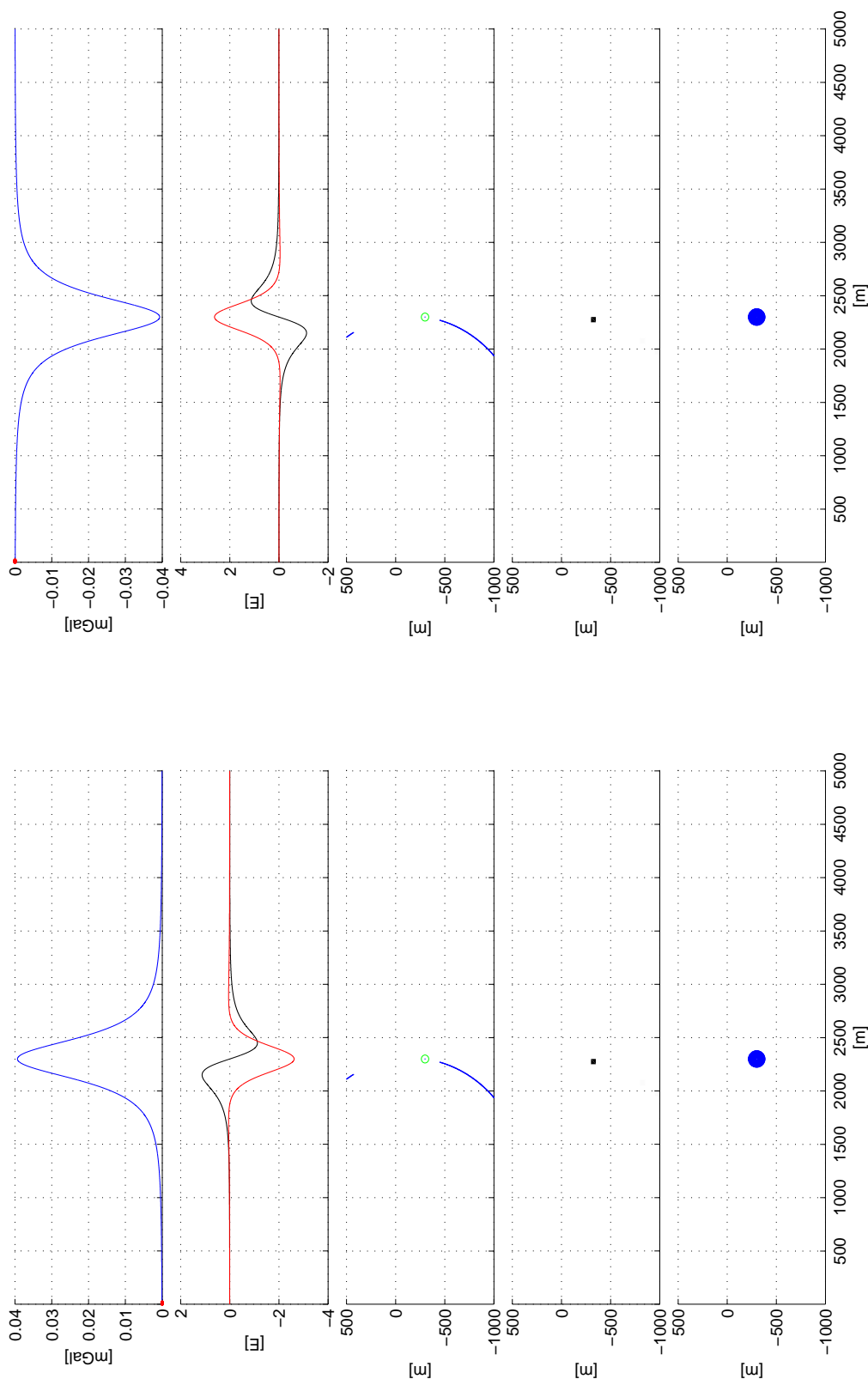


Figure 3.2: Single point mass anomaly, positive $\Delta\rho$.

Figure 3.3: Single point mass anomaly, negative $\Delta\rho$.

For further explanations of the figures please refer to page 32.

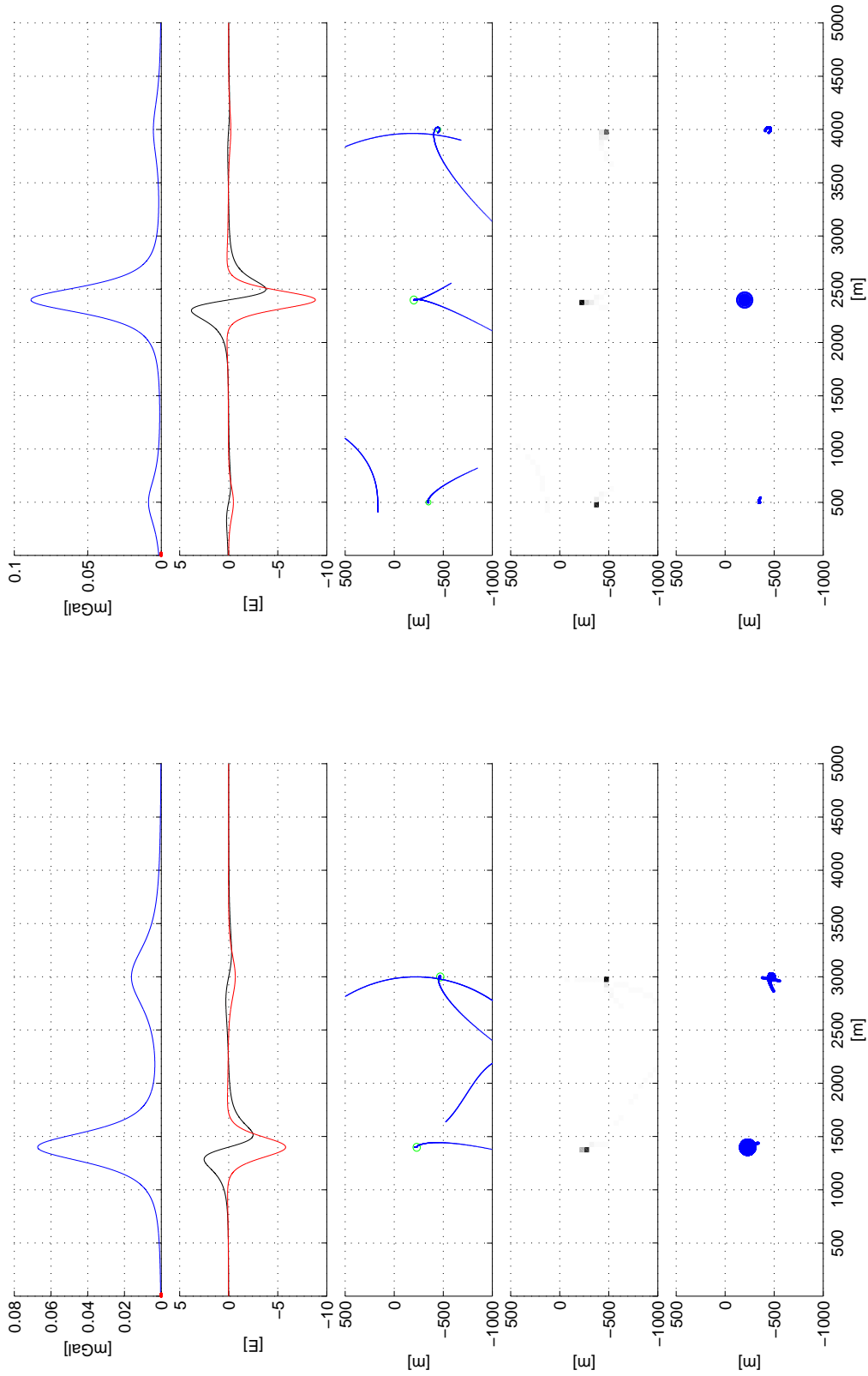


Figure 3.4: Two point masses.

Figure 3.5: Three point masses.

For further explanations of the figures please refer to page 32.

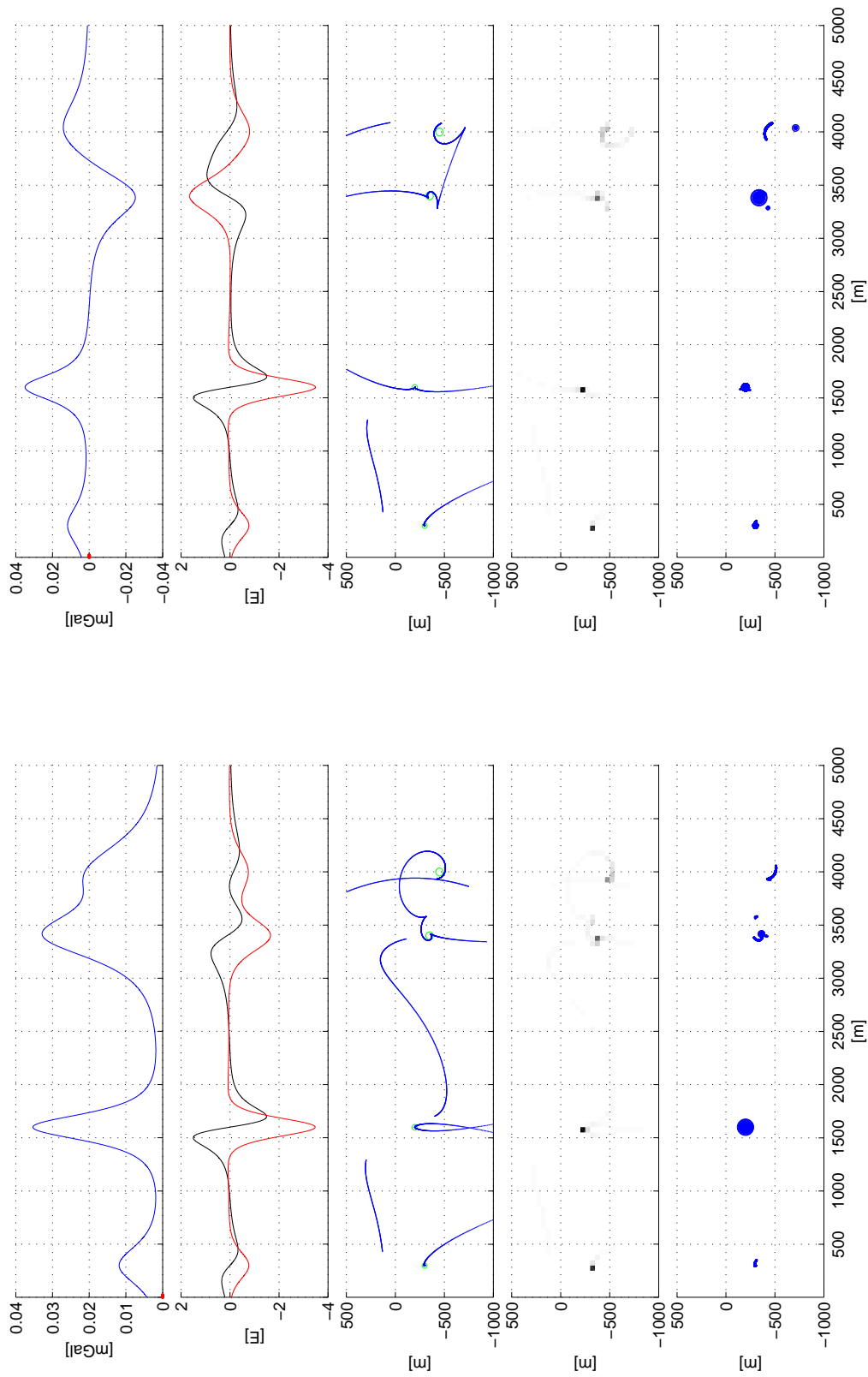


Figure 3.6: Four point masses.

Figure 3.7: Four point masses, second to the right with negative $\Delta\rho$.

For further explanations of the figures please refer to page 32.

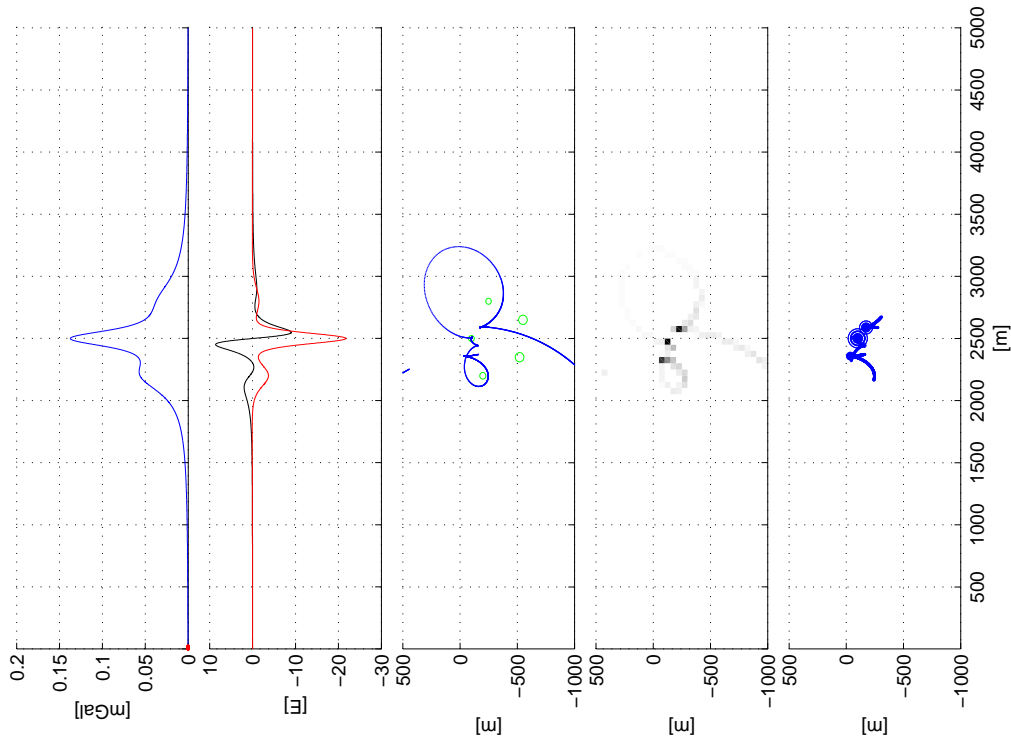


Figure 3.8: Five strongly lumped point masses.

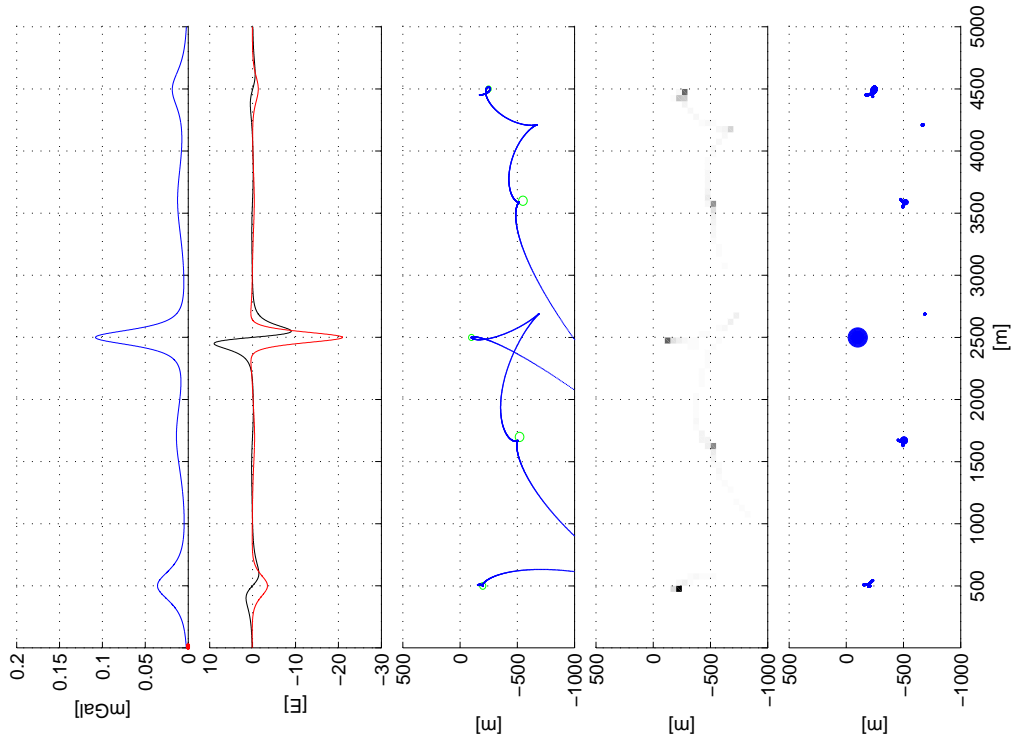


Figure 3.9: Five masses with the same size and at the same depth.

For further explanations of the figures please refer to page 32.

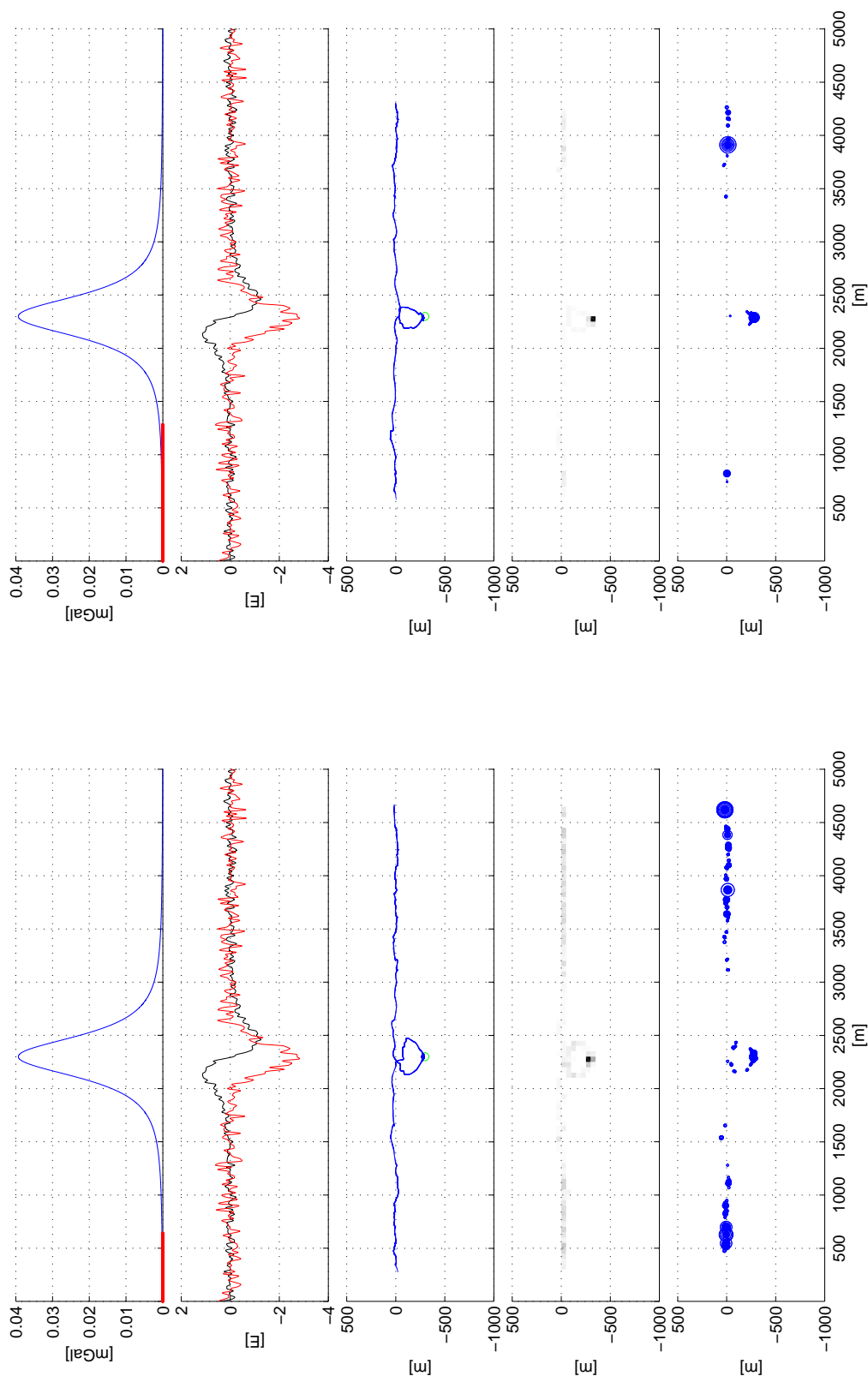


Figure 3.10: One point mass, 10% noise, window size of 641 samples.

Figure 3.11: One point mass, 10% noise, window size of 1281 samples.

For further explanations of the figures please refer to page 32.

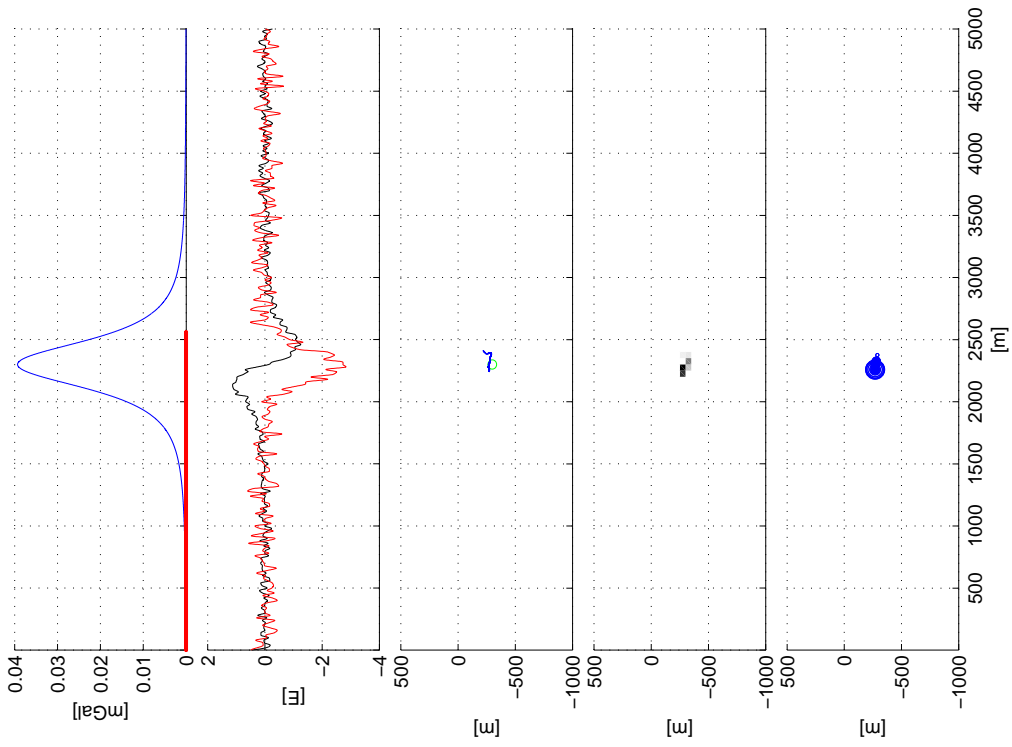


Figure 3.12: One point mass, 10% noise, window size of 2561 samples.

For further explanations of the figures please refer to page 32.

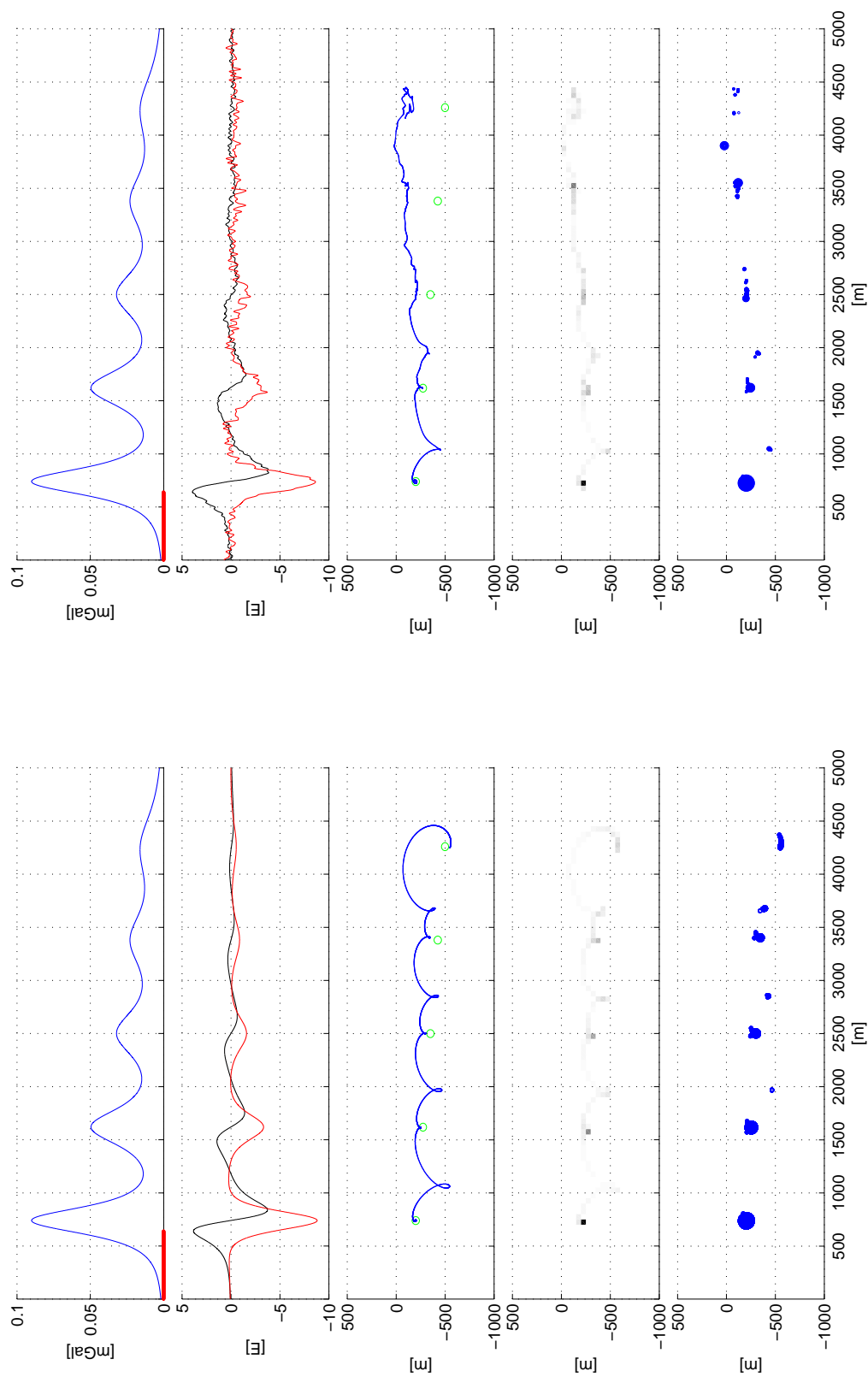


Figure 3.13: Five point masses with same size, different depth, noiseless, window size of 641 samples.

Figure 3.14: Five point masses with same size, different depth, 10% noise, window size of 641 samples.

For further explanations of the figures please refer to page 32.

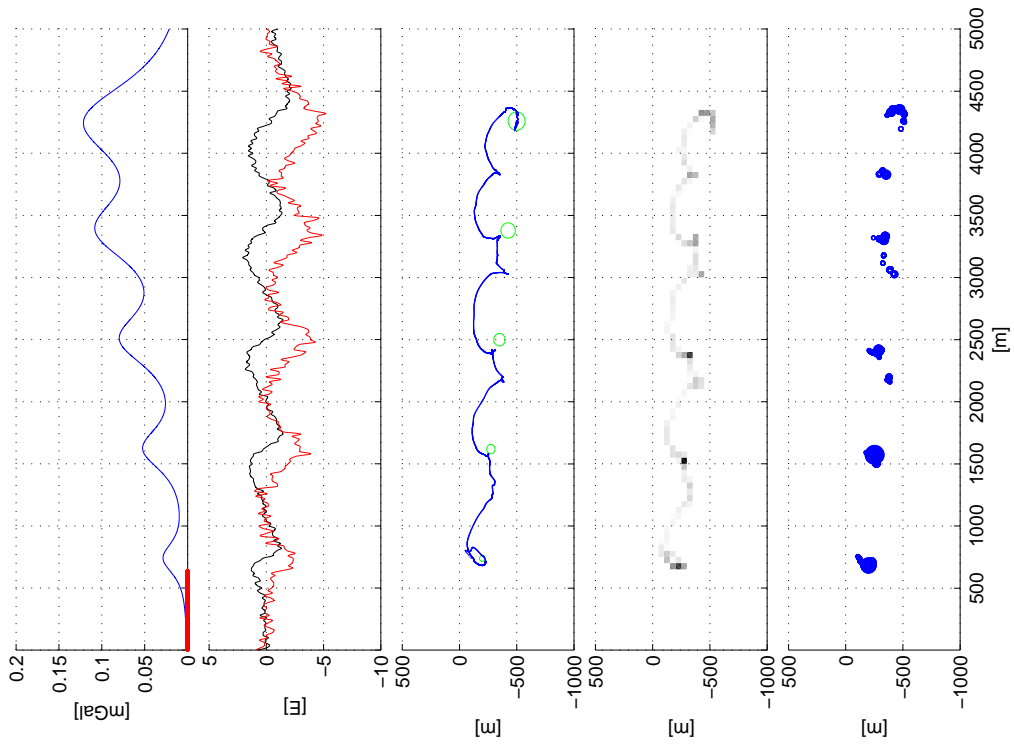


Figure 3.15: Five point masses, size bigger with depth, 10% noise, window size of 641 samples.

For further explanations of the figures please refer to page 32.

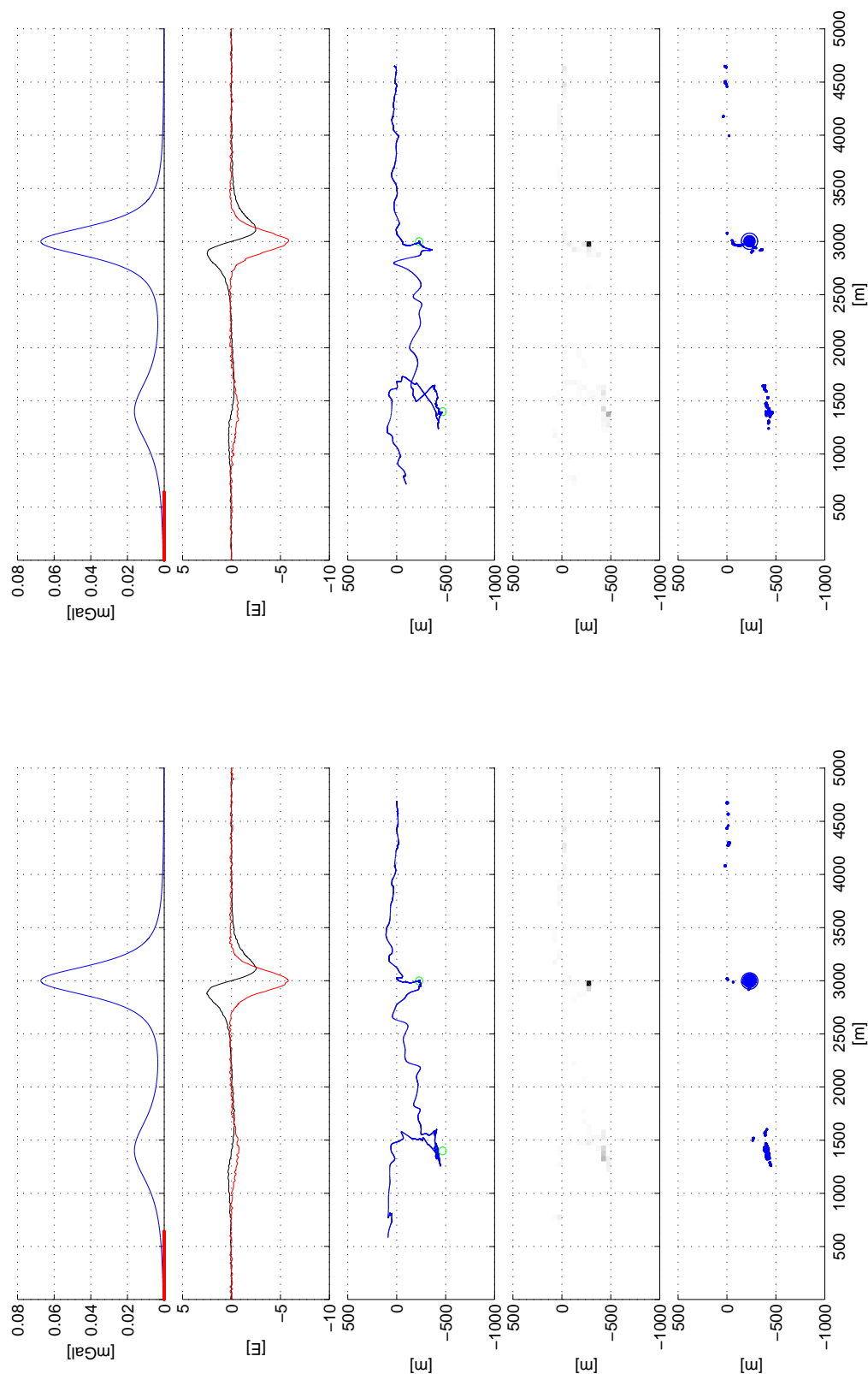


Figure 3.16: Two point masses, 10% noise.

Figure 3.17: Two point masses, different noise at 10%.

For further explanations of the figures please refer to page 32.

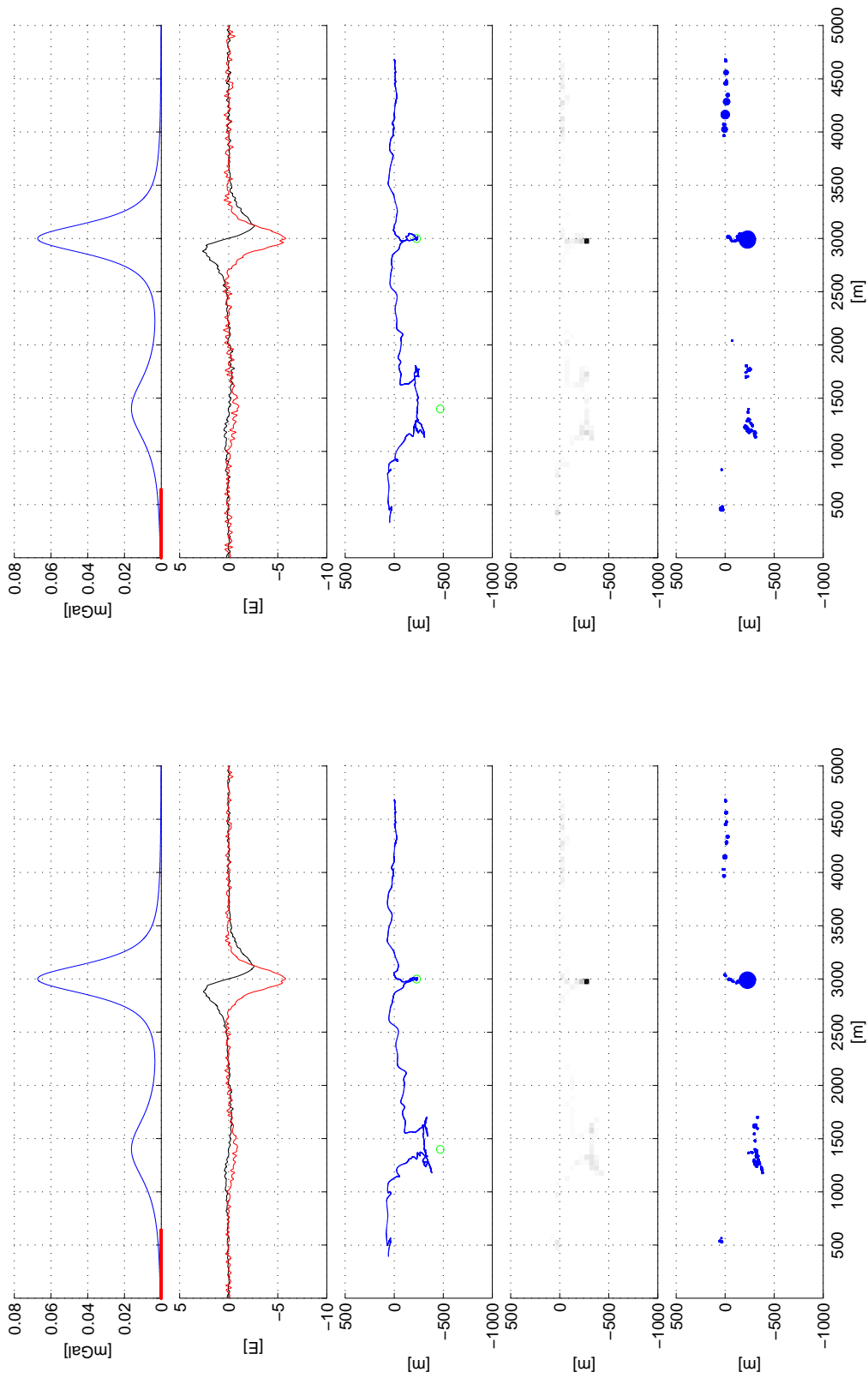


Figure 3.18: Two point masses, 20% noise.

Figure 3.19: Two point masses, 30% noise.

For further explanations of the figures please refer to page 32.

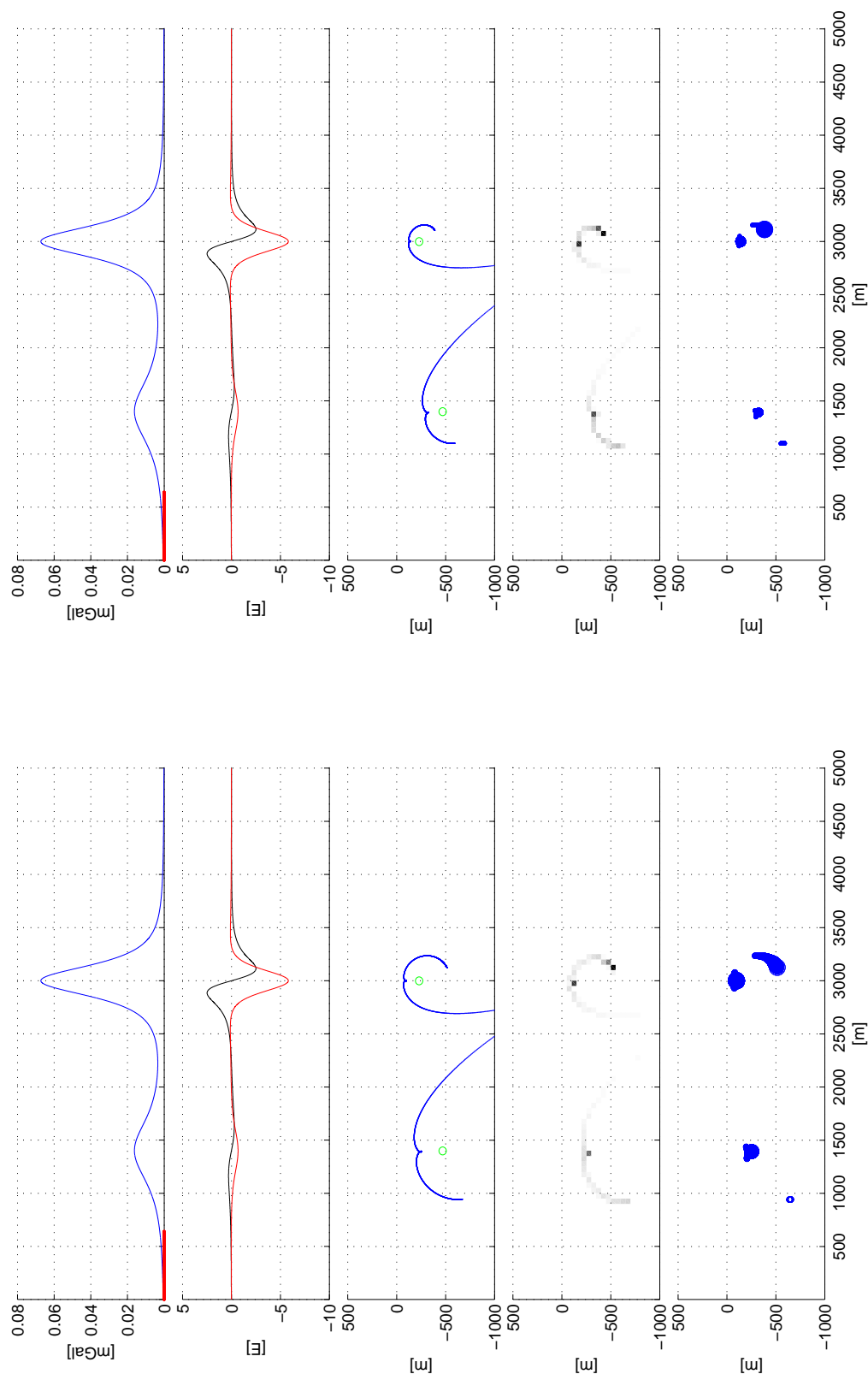


Figure 3.21: Two point masses, $n = 1$

Figure 3.20: Two point masses, $n = 0.5$

For further explanations of the figures please refer to page 32.

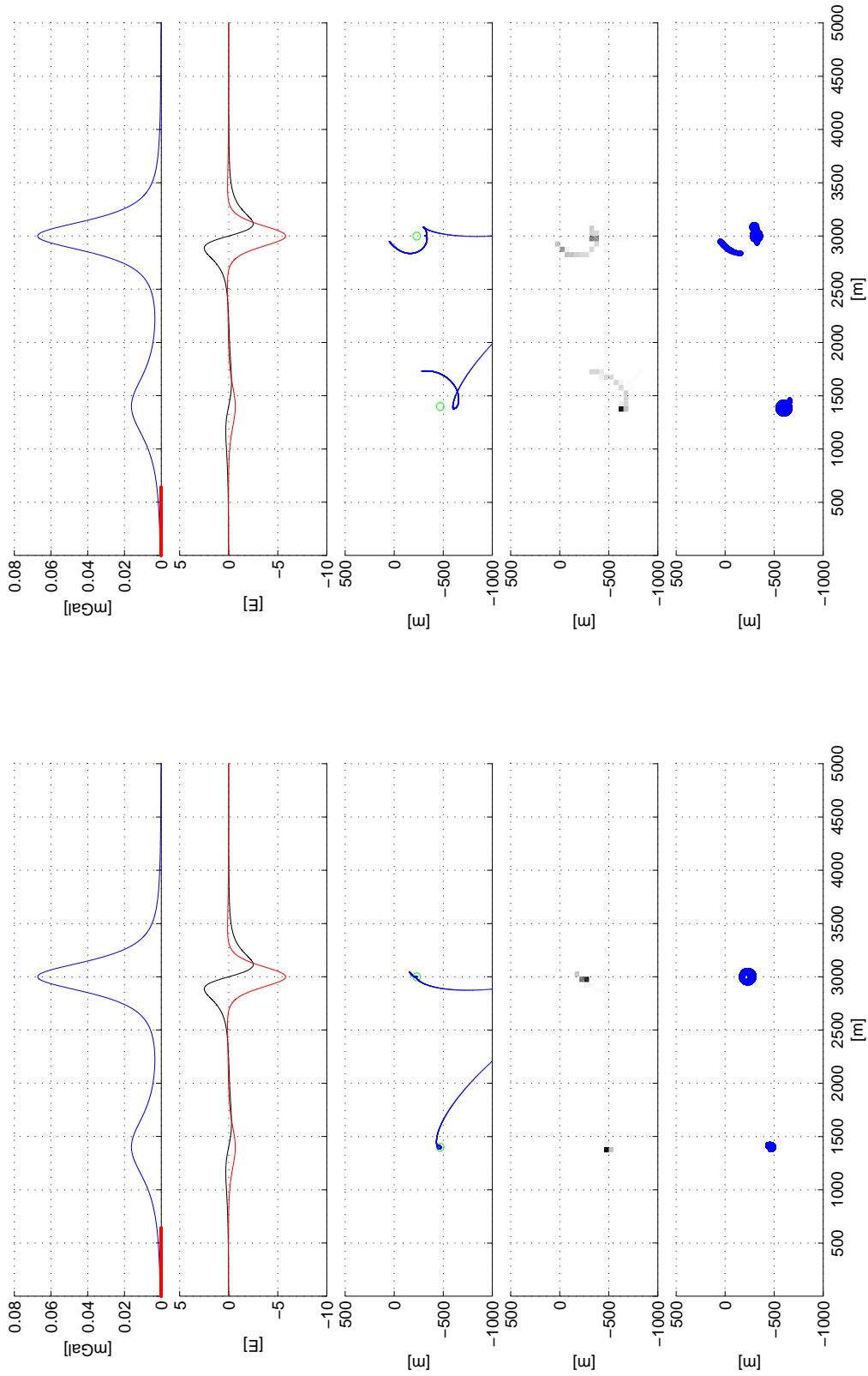


Figure 3.22: Two point masses, $n = 2$

Figure 3.23: Two point masses, $n = 3$

For further explanations of the figures please refer to page 32.

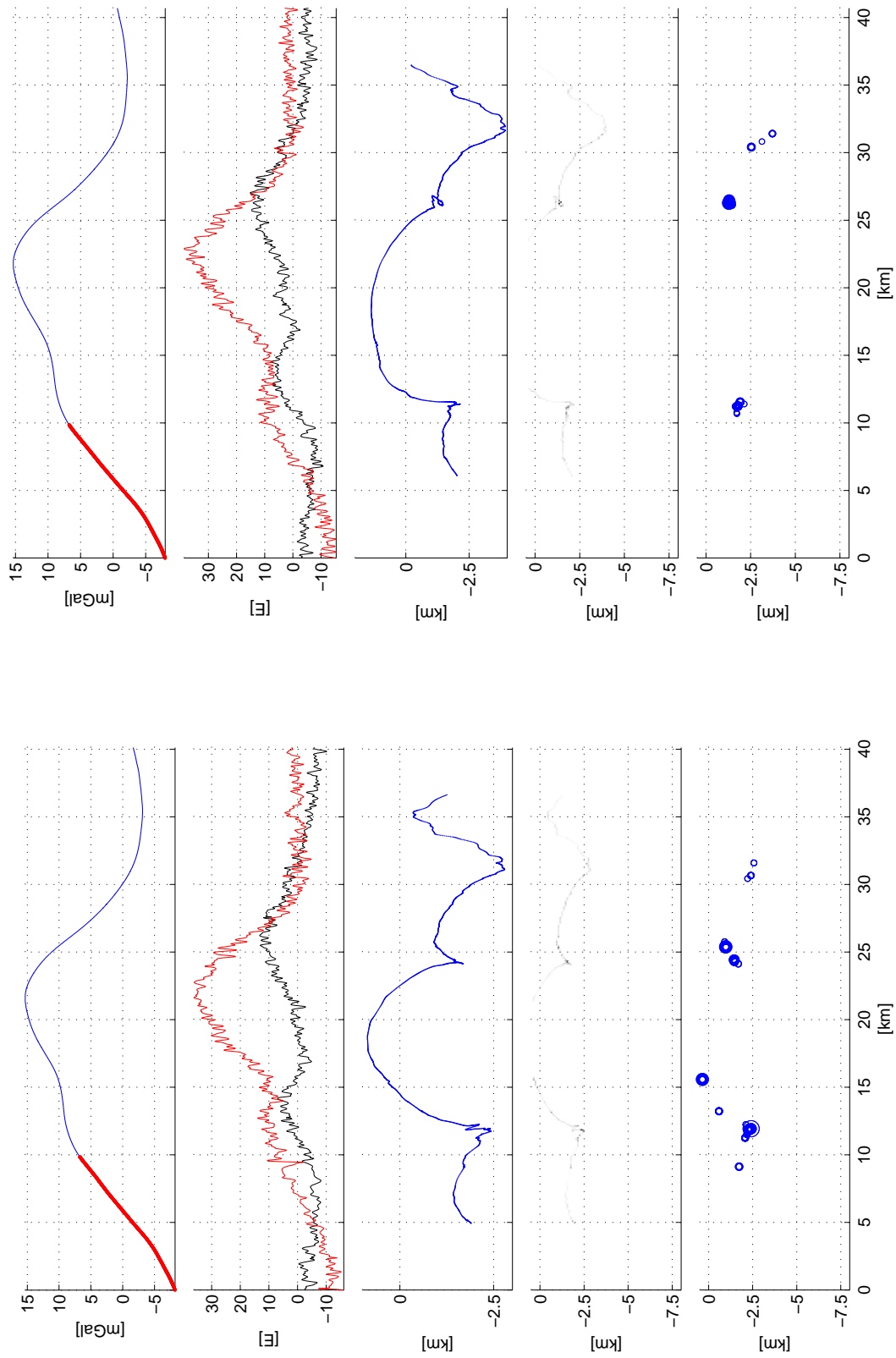


Figure 3.24: Raw data, line 53, window size of 1001 samples.

Figure 3.25: Raw data, line 54, window size of 1001 samples.

For further explanations of the figures please refer to page 32.

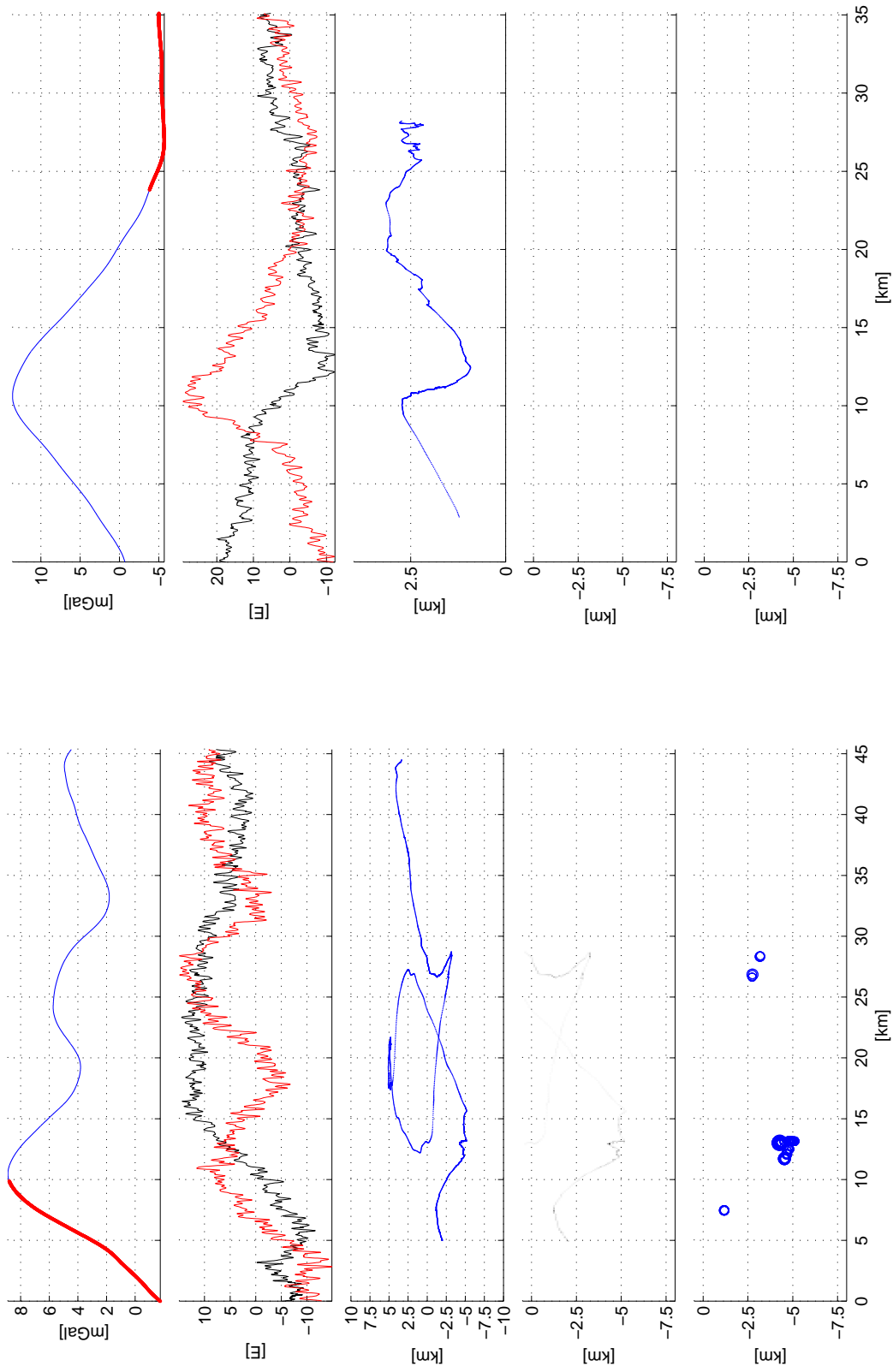


Figure 3.26: Raw data, line 65, window size of 1001 samples.

Figure 3.27: Raw data, tie 40, window size of 1001 samples.

For further explanations of the figures please refer to page 32.

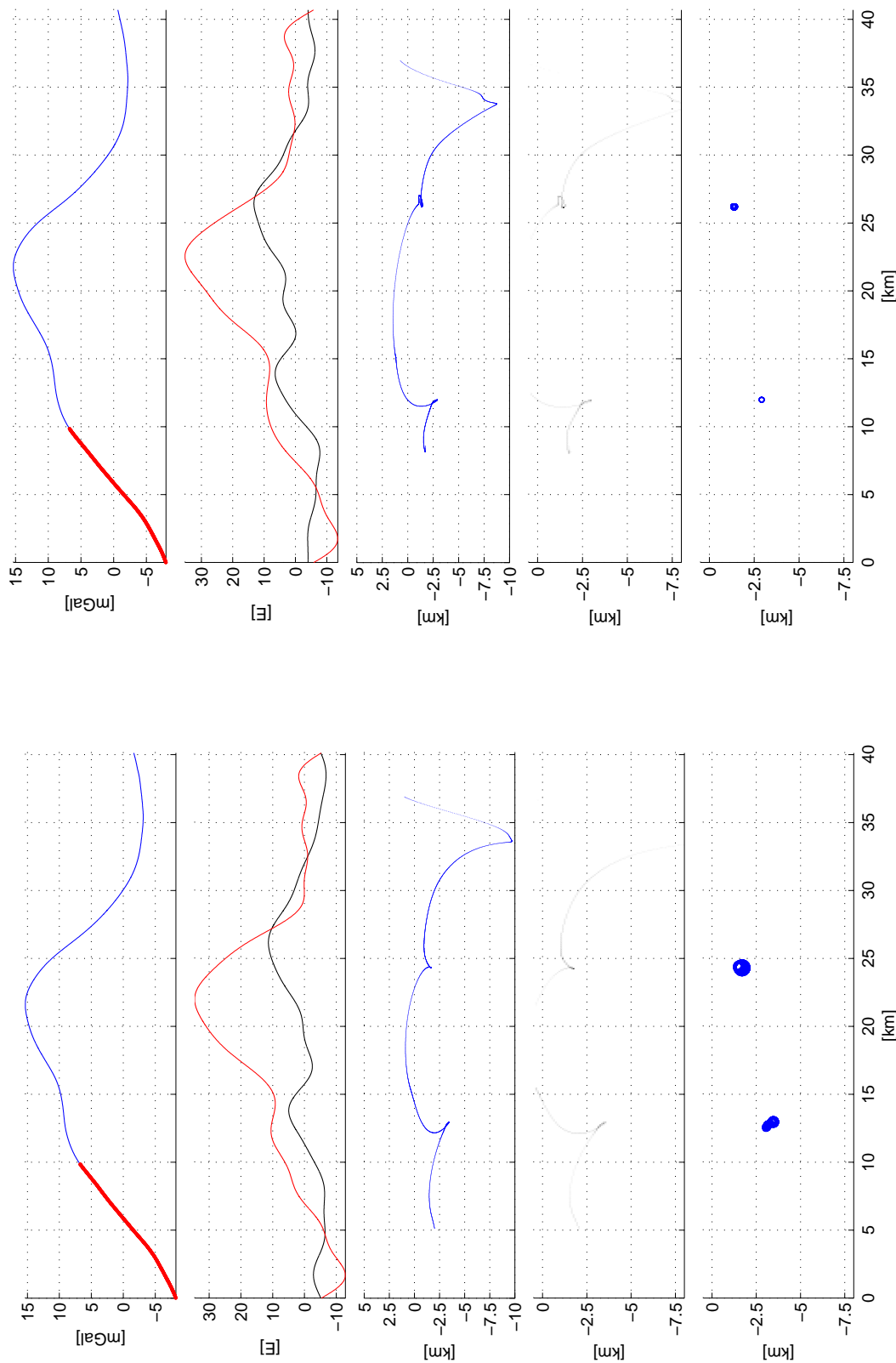


Figure 3.29: Smoothed data, line 54, window size of 1001 samples.

Figure 3.28: Smoothed data, line 53, window size of 1001 samples.

For further explanations of the figures please refer to page 32.

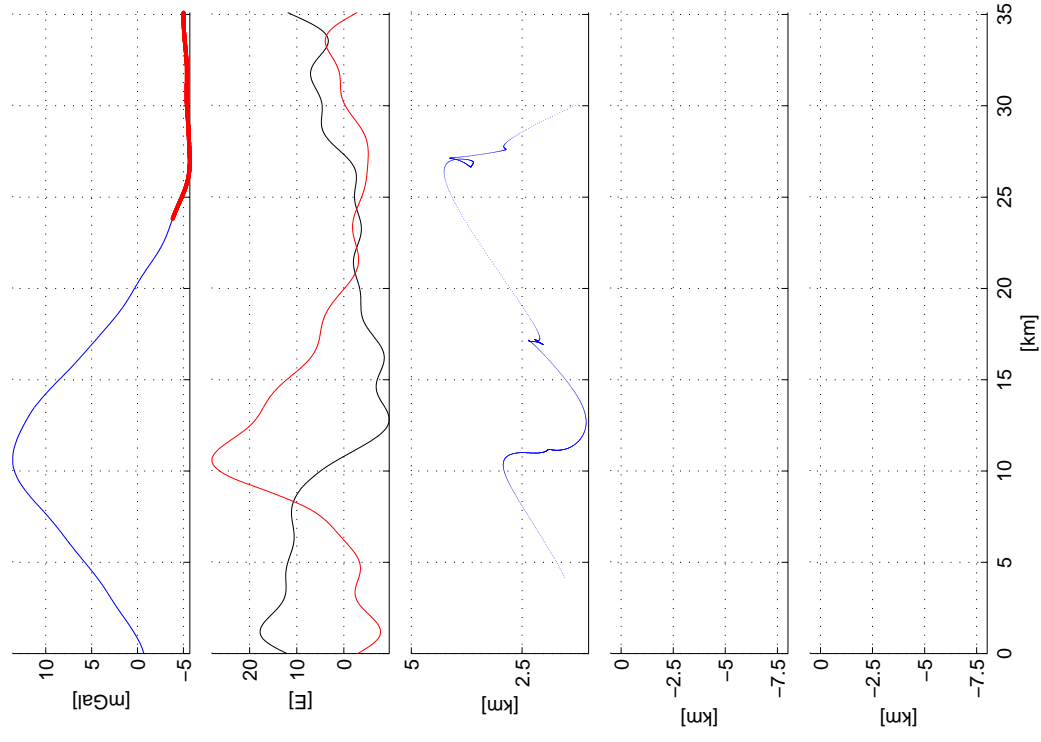


Figure 3.30: Smoothed data, line 65, window size of 1001 samples.

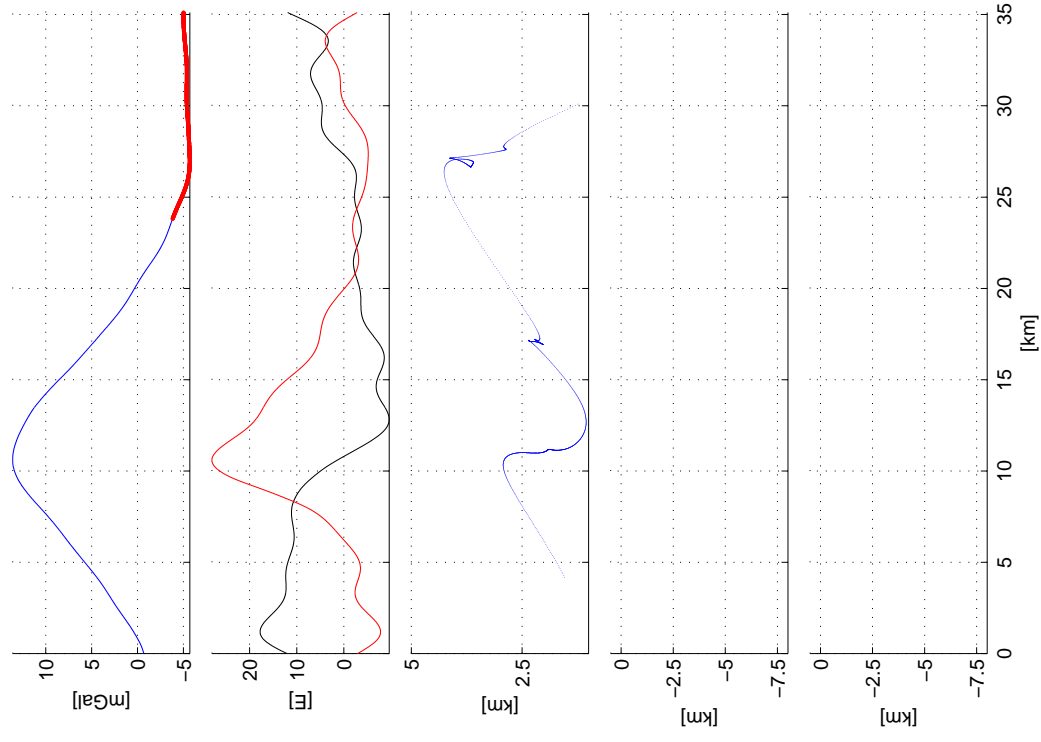


Figure 3.31: Smoothed data, tie 40, window size of 1001 samples.

Chapter 4

Conclusions

The fact that the data is preprocessed is limiting the analysis as some tests for data integrity and accuracy cannot be used (e. g. Laplace's equation). Also it is not known in detail how the measurement data were preprocessed to get the actual gravity gradient data.

The Euler deconvolution is a good method to identify possible locations of interesting mass bodies. Hereby no difference is made whether the mass anomaly is negative or positive.

It is possible to detect several bodies in a measurement area if the bodies are sufficiently distinct. How much distance has to be between bodies depends on the depth and the size of the bodies.

Also the measurement area has to contain the whole signal of the mass anomaly. It benefits this analysis that the mass anomaly of the examined data set appears clearly in the data. But the anomaly is almost too big to perform the Euler deconvolution well, respectively the surveyed area is too small.

Noise is a problem for the Euler deconvolution and disturbs the interpretation as the solutions will not cluster well. Smoothing the data shows an effect to a certain extent but does not help that much. The solutions of the Euler deconvolution tend to cluster around a mass center. The more noise in the data occurs the more loose a cluster is formed and it becomes more difficult to identify this cluster as a possible location for a mass anomaly.

An Euler deconvolution with a smaller window size produces more "ghost masses" while it "overlooks" smaller structures with a bigger window size more easily. Therefore a compromise between the number of false positives and the size of the detected mass anomalies must be made. The window size should be chosen to match the size of the expected mass anomaly. Additionally the expected depth of the body must be taken into account: the signal gets shallower and broadens with the depth of the body. As the signal broadens the window size should increase.

The Euler deconvolution works best if the structural index n matches the form of the source (e. g. sphere, prism, cylinder etc.) and the form of the source matches the used equations. In more realistic cases n may be not a constant. As well as a natural source does not form a perfect geometrical body.

It is possible to compute the Euler deconvolution with the full gravity gradient tensor. The full gravity gradient tensor provides more measurement values on a single measurement point and therefore helps in finding better solutions.

As the research progresses enhancements to the Euler deconvolution are found, e. g. to improve the accuracy and to determine multiple structural indices at once (Cooper, 2008), to distinguish reliable solutions from spurious ones (FitzGerald et al., 2004) or to make usage of different geometries of the mass anomalies (Zhang et al., 2000).

Other approaches to enhance the Euler deconvolution can be found surely. But also the measurement devices could be enhanced if one finds the sources of the noise and then a suitable way to eliminate the noise.

If other data are available which may be analyzed by other methods, the solutions of the Euler deconvolution can be cross verified. This benefits its plausibility.

Bibliography

- Bell Geospace (2009), 'Full tensor gravity gradiometry – technology overview', Webpage.
 URL: <http://www.bellgeo.com>
- Blakely, R. J. (1995), *Potential Theory in Gravity and Magnetic Applications*, Cambridge University Press.
- Cooper, G. R. J. (2008), 'Euler deconvolution with improved accuracy and multiple different structural indices', *Journal of China University of Geosciences* **19**(1), 72–76.
- FitzGerald, D., Reid, A. and Philip, M. (2004), 'New discrimination techniques for euler deconvolution', *Computers & Geosciences* **30**, 461–469.
- Hatch, D. (2004), Evaluation of a full tensor gravity gradiometer for kimberlite exploration, in R. J. L. Lane, ed., 'Airborne Gravity 2004 – Abstracts from the ASEG-PESA Airborne Gravity 2004 Workshop', Vol. 18, Geoscience Australia, pp. 73–79.
- Murphy, C. A. (2004), The Air-FTGTM airborne gravity gradiometer system, in R. J. L. Lane, ed., 'Airborne Gravity 2004 – Abstracts from the ASEG-PESA Airborne Gravity 2004 Workshop', Vol. 18, Geoscience Australia, pp. 7–14.
- Mushayandevu, M. F., Lesur, V., Reid, A. B. and Fairhead, J. D. (2004), 'Grid euler deconvolution with constraints for 2d structures', *Geophysics* **69**(2), 489–496.
- Råde, L. and Westergren, B. (1995), *Springers Mathematische Formeln*, Springer-Verlag Berlin Heidelberg.
- Rummel, R. (1986), *Lecture Notes in Earth Sciences*, Vol. 7, Springer-Verlag Berlin Heidelberg, chapter Satellite Gradiometry, pp. 317–363.
- Sedgewick, R. (1992), *Algorithmen*, Addison-Wesley.
- Smallwood, J. R., Towns, M. J. and White, R. S. (2001), 'The structure of the Faeroe-Shetland Trough from integrated deep seismic and potential field modelling', *Journal of the Geological Society* v. **158**/3, 409–412.
- Torge, W. (1989), *Gravimetry*, de Gruyter.
- Wu, P. (2007), 'Euler deconvolution'.
 URL: <http://www.geo.ucalgary.ca/wu/Goph547/EulerDeconvolution.pdf>
- Zhang, C., Mushayandevu, M. F., Reid, A. B., Fairhead, J. D. and Odegard, M. E. (2000), 'Euler deconvolution of gravity tensor gradient data', *Geophysics* **65**, 512–520.

Appendix A

In the Appendix the MATLAB source code filenames will be listed with a short explanation what each file does.

All the MATLAB source codes as well as the gravity gradiometry data set have the directory `matlab` as root directory.

A.1 Gradient tensor

(in directory `synth_gradient_tensor`)

- `tensor_point_mass.m` – main component, computes a gradient tensor for a single point mass

A.2 Data set

A.2.1 Coarse analysis

(in directory `datensatz`)

- `showdata.m` – main component, analysis of the data set
- `ausgleichende_gerade.m` – fits a straight line to each trajectory
- `distlintiepoi.m` – computes the distances between lines, ties ans measurement points
- `gauss_area.m` – computes the area of the convex hull of the measurement area
- `interpol_data_to_raster.m` – interpolates the data to a raster
- `interpoliere.m` – helper function for `interpol_data_to_raster.m`
- `latex_out.m` – outputs a formatted string into a file
- `least_diffs.m` – computes the least distance from the fitted line to the original measurement point location
- `read_bell_data.m` – reads the original data set (ASCII file) into Matlab
- `redblue.m` – helper function to generate some color tables
- `Line53.m` – main component, some analysis of line no. 53

- `glaetten.m` – main component, smoothes all data with a low pass filter (FFT-IFFT operation while cutting off high frequencies)

A.2.2 Crossover analysis

(in directory `crossover`)

- `crossover_analysis.m` – main component, crossover analysis of the data set
- `ausgleichende_gerade.m` – same as above
- `crosspoint.m` – computes crosspoint
- `crosspoint_neighbors.m` – identifies four points next to an crosspoint
- `is_intersect.m` – proofs on intersection
- `points_near_crosspoint.m` – gets all points in a radius around a crosspoint

A.3 Euler Deconvolution

A.3.1 2D – synthetic data

(in directory `euler_synth`)

- `testeuler.m` – main component
- `datagen2D.m` – generates test data
- `euler_synth.m` – helper function to analyse the data of the Euler Deconvolution
- `EulerDeconv_2D_all.m` – 2D Euler Deconvolution
- `gather.m` – gathers all data in a 2D raster
- `slowrandn.m` – computes long wavelength noise

A.3.2 Euler Deconvolution with real data

(in directory `euler_meas`)

- `show_lines.m` – main component, shows the location of the chosen lines
- `testeuler_meas.m` – main component, loads the data of the chosen lines
- `euler_meas.m` – skript to do the Euler Deconvolution and the figure
- `EulerDeconv_2D_all.m` – as before
- `gather.m` – as before
- `redblue.m` – as before